

Thermally reconfigurable monoclinic nematic colloidal fluids

<https://doi.org/10.1038/s41586-021-03249-0>

Haridas Mundoor¹, Jin-Sheng Wu², Henricus H. Wensink³ & Ivan I. Smalyukh^{1,2,4,5}✉

Received: 19 July 2020

Accepted: 26 November 2020

Published online: 10 February 2021

 Check for updates

Fundamental relationships are believed to exist between the symmetries of building blocks and the condensed matter phases that they form¹. For example, constituent molecular and colloidal rods and disks impart their uniaxial symmetry onto nematic liquid crystals, such as those used in displays^{1,2}. Low-symmetry organizations could form in mixtures of rods and disks^{3–5}, but entropy tends to phase-separate them at the molecular and colloidal scales, whereas strong elasticity-mediated interactions drive the formation of chains and crystals in nematic colloids^{6–11}. To have a structure with few or no symmetry operations apart from trivial ones has so far been demonstrated to be a property of solids alone¹, but not of their fully fluid condensed matter counterparts, even though such symmetries have been considered theoretically^{12–15} and observed in magnetic colloids¹⁶. Here we show that dispersing highly anisotropic charged colloidal disks in a nematic host composed of molecular rods provides a platform for observing many low-symmetry phases. Depending on the temperature, concentration and surface charge of the disks, we find nematic, smectic and columnar organizations with symmetries ranging from uniaxial^{1,2} to orthorhombic^{17–21} and monoclinic^{12–15}. With increasing temperature, we observe unusual transitions from less- to more-ordered states and re-entrant²² phases. Most importantly, we demonstrate the presence of reconfigurable monoclinic colloidal nematic order, as well as the possibility of thermal and magnetic control of low-symmetry self-assembly^{2,23,24}. Our experimental findings are supported by theoretical modelling of the colloidal interactions between disks in the nematic host and may provide a route towards realizing many low-symmetry condensed matter phases in systems with building blocks of dissimilar shapes and sizes, as well as their technological applications.

Experimental design and emergent behaviour

We report the emergence of monoclinic and orthorhombic orientational order in dispersions of thin colloidal disks within a nematic liquid crystal (LC) composed of rodlike molecules, in which both molecular and colloidal components lack such symmetry properties of their own. Competing electrostatic and elastic interactions interplay with the temperature-dependent boundary conditions on the colloidal surfaces so that the disks rotate relative to the LC host with changing temperature, transforming the symmetry of the ensuing nematic colloidal building blocks and reconfiguring their interactions (Fig. 1a–c). To unambiguously demonstrate the self-assembly of these LC colloids into monoclinic nematic and other low-symmetry states, we directly characterize them using three-dimensional (3D) optical imaging through selective excitation of the disks and molecules by a tunable femtosecond laser. The average local orientation of the long axes of the rodlike molecules of the nematic host pentylcyanobiphenyl (5CB), described by a molecular director \mathbf{n}_m , is probed by exploiting the strong polarization dependence of three-photon excitation

fluorescence from 5CB (Extended Data Fig. 1a). The β -NaYF₄:Yb/Er disks with strong photon-upconverting luminescence are designed to allow for probing their orientations and positions (Fig. 1a, Extended Data Fig. 1b–l) via direct confocal imaging. Highly anisotropic disks are stabilized against aggregation through surface functionalization, which also imparts self-reconfigurability of boundary conditions at their surfaces. To this end, hydrothermally synthesized 10-nm-thick disks of diameter controlled within $D = 1.2$ – $2.2 \mu\text{m}$ are coated with thin ($\leq 5 \text{ nm}$) silica layers and then functionalized with polyethylene glycol (Fig. 1a, Extended Data Fig. 1b–e)^{10,25,26}. The disk charge in 5CB with a Debye screening length of $\xi_D = 0.1$ – $0.5 \mu\text{m}$ is controlled within $Z^*e \approx +(0$ – $100)e$ (Z^* is the effective number of elementary charges e)¹⁰ and characterized using electrophoretic colloidal mobility (Extended Data Fig. 1m–o). Dispersions of disks in 5CB are infiltrated into glass cells, rectangular capillaries or microfabricated containers of various micrometre-to-inch dimensions, with the inner surfaces treated to impose strong perpendicular or tangential boundary conditions for \mathbf{n}_m . Confocal cross-sectional imaging planes are then aligned relative to the symmetry axes of the colloidal dispersions. 3D imaging

¹Department of Physics, University of Colorado, Boulder, CO, USA. ²Chemical Physics Program, Departments of Chemistry and Physics, University of Colorado, Boulder, CO, USA.

³Laboratoire de Physique des Solides, CNRS, Université Paris-Saclay, Orsay, France. ⁴Materials Science and Engineering Program, Department of Electrical, Computer, and Energy Engineering, University of Colorado, Boulder, CO, USA. ⁵Renewable and Sustainable Energy Institute, National Renewable Energy Laboratory and University of Colorado, Boulder, CO, USA.

✉e-mail: ivan.smalyukh@colorado.edu

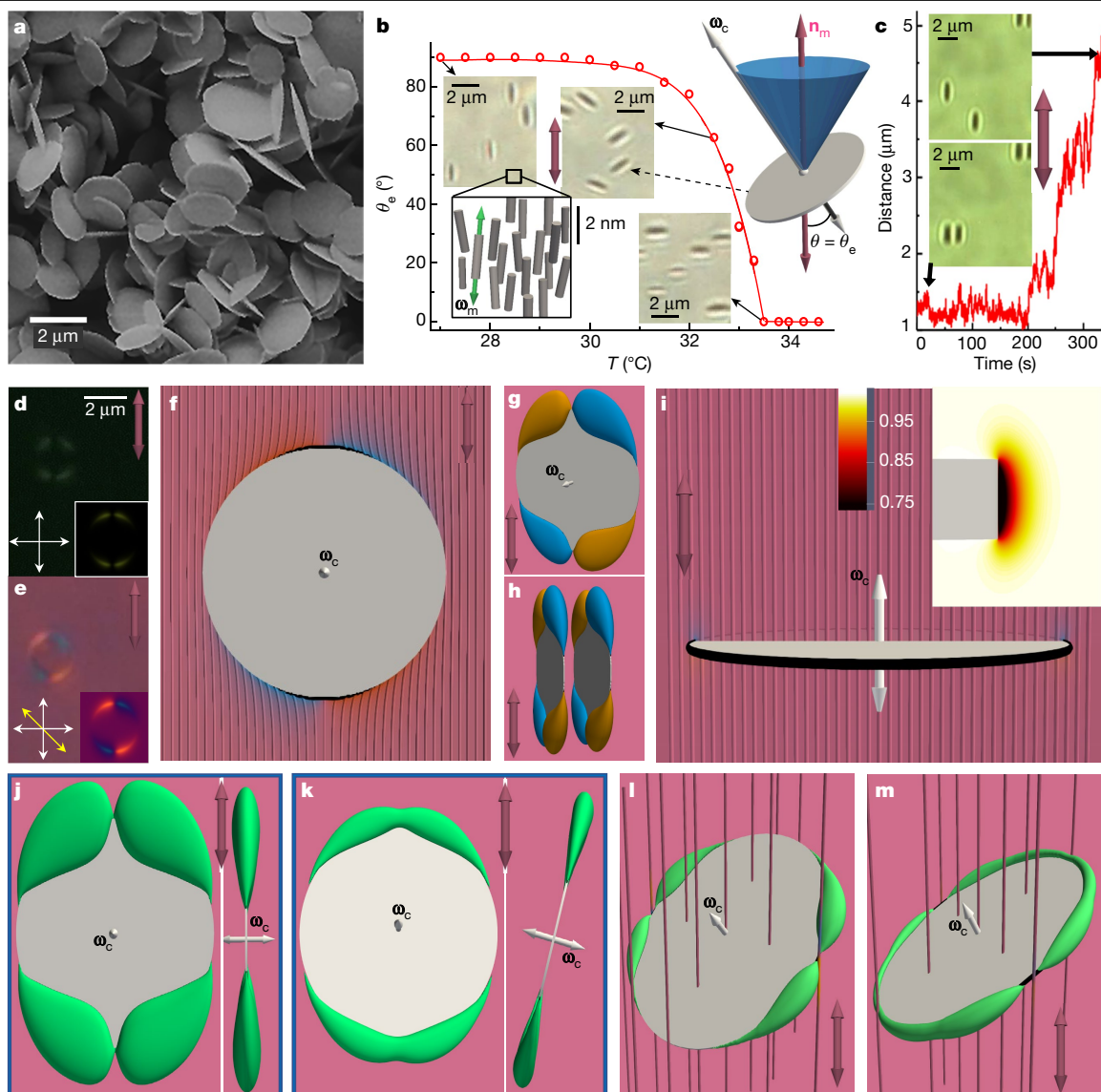


Fig. 1 | Colloidal disks in a nematic host of molecular rods. **a**, Scanning electron micrograph of as-synthesized disks. **b**, Angle θ_e between the disk normal ω_c and the molecular director \mathbf{n}_m , as defined in the top-right inset, versus temperature T at $Z^*e \approx +80e$, with a theoretical fit (red curve) of the experimental data (circles) using $\cos\theta_e = W_f/[1 - (1+W_f)^{(T-T_c)/(T_0-T_c)}]$ for $T > T_c$, $T_0 = 33.5 \pm 0.1^\circ\text{C}$, $T_c = 29.5 \pm 0.1^\circ\text{C}$ and $W_f = 0.06 \pm 0.03$ (Supplementary Information). Left-side insets show bright-field micrographs with different disk orientations and a pictorial representation of 5CB molecules with long axes ω_m within the LC. **c**, Centre-to-centre inter-disk distance versus time, showing how thermal fluctuations dissociate disks that were weakly ‘bound at a distance’. Insets show bright-field micrographs for the initial and final positions. **d, e**, Polarizing optical micrographs of disks in 5CB at $\theta_e = 90^\circ$, obtained between crossed polarizers

(white double arrows) without (**d**) and with (**e**) a 530-nm retardation plate (slow axis shown by a yellow double arrow). Insets present their computer-simulated counterparts. **f–h**, Computer-simulated distortions of \mathbf{n}_m around a disk at $\theta_e = 90^\circ$. Orange and blue colouring of lines in **f** shows the local \mathbf{n}_m directions of tilting, matching the ones revealed experimentally in **e**. Coloured isosurfaces in **g, h** depict regions where \mathbf{n}_m -departures away from its far-field background (pink double arrows) are $>3^\circ$ in opposite directions (different colours) within the plane containing the midplane of the disk. Black isosurfaces show regions near disk edges where S_m is reduced by $\geq 5\%$. **i**, Regions of reduced S_m and \mathbf{n}_m structure at $\theta_e = 0^\circ$. The inset shows details of colour-coded S_m at the disk edge, scaled by its equilibrium bulk value. **j–m**, Green colour shows isosurfaces of \mathbf{n}_m deformations by $>3^\circ$ in all directions around disks at $\theta_e = 90^\circ$ (**j**), 75° (**k**), 45° (**l**) and 30° (**m**).

with resolution <500 nm resolves individual disks within different phases (Supplementary Videos 1–3), and image analysis reveals their positions and orientations relative to \mathbf{n}_m with a precision of 10–50 nm and 1° – 2° , respectively, depending on the imaging depth. This direct 3D imaging of disks unambiguously probes purely orientational order in optically biaxial^{12–21} monoclinic and orthorhombic nematic colloidal phases and also positional order in smectic and columnar phases.

Self-alignment and interactions of disks

Colloidal particles locally distort the molecular nematic order because of anisotropic interactions at their surfaces, which for microparticles

result in singular topological defects (Extended Data Fig. 2a) and strong elasticity-mediated interactions with binding energies that are thousands of times greater than the thermal energy^{6,7}. Polarizing microscopy and numerical modelling consistently reveal only weak perturbations of the nematic order around thin disks with soft boundary conditions and large-area faces parallel to the far-field \mathbf{n}_m (Fig. 1d–g). Close to disk edges, \mathbf{n}_m locally departs from its uniform far-field background by a few degrees, and the molecular scalar order parameter $S_m = \langle 3(\omega_m \cdot \mathbf{n}_m)^2 - 1 \rangle / 2$ decreases by only a few per cent relative to its equilibrium bulk value (Fig. 1f), so that reduction of the latter cannot be detected with bright-field imaging (Extended Data Fig. 2a); ω_m and $\langle \rangle$ denote the symmetry axis of each molecular rod

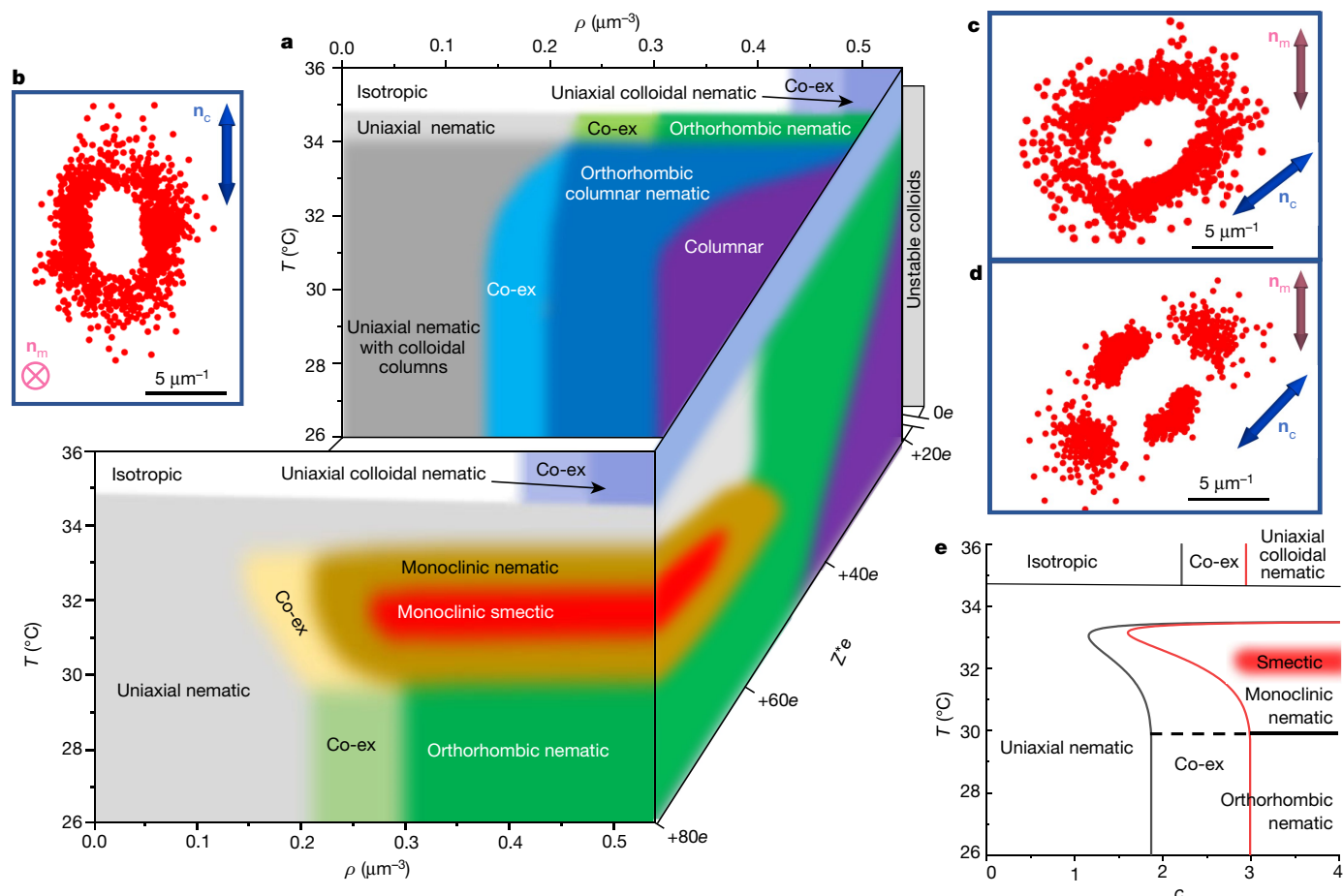


Fig. 2 | Phase diagrams and characterization of phases. **a**, Diagram of the hybrid LC phases upon variation of the disk number density ρ , temperature T and colloidal charge Z^*e . ‘Co-ex’ refers to co-existence regions between neighbouring phases. Disks aggregate at $Z^*e < +10e$ when nemato-elastic attractions overpower electrostatic repulsions; Wigner-type crystals form at $Z^*e > +100e$ (ref. ¹⁰). Formation of colloidal columns within the uniaxial nematic at $Z^*e = +20e$ becomes progressively slower with decreasing ρ , but dimers and short columns are found starting from $\rho \approx 0.01 \mu\text{m}^{-3}$ at room temperature (Fig. 1c). T is measured with an error of $\pm 0.1^\circ\text{C}$; relative errors of estimating ρ

and Z^*e are $\pm 5\%$ and $\pm 1\%$, respectively (as described for the corresponding experimental measurements in Methods). **b–d**, Fourier analysis of pairwise colloidal positions in an orthorhombic nematic at $\rho = 0.34 \mu\text{m}^{-3}$, $T = 27.0 \pm 0.1^\circ\text{C}$ (**b**), monoclinic nematic at $\rho = 0.31 \mu\text{m}^{-3}$, $T = 30.7 \pm 0.1^\circ\text{C}$ (**c**) and monoclinic smectic at $\rho = 0.29 \mu\text{m}^{-3}$, $T = 31.7 \pm 0.1^\circ\text{C}$ (**d**). The Fourier analysis is based on 3D imaging and tracking of disk positions with an error of $< 50 \text{ nm}$. **e**, Theoretical phase diagram of T versus dimensionless concentration, $c = \rho D^3 \pi^2 / 16$, for $Z^*e \approx +80e$, corresponding to its experimental counterpart in **a**.

and an ensemble average, respectively (Fig. 1b). Electrostatic repulsions between like-charged disks at $Z^*e > +50e$ overpower anisotropic elastic interactions that attract regions of the same particle-induced tilt of \mathbf{n}_m relative to its uniform background (orange/blue colours in Fig. 1e–h) to minimize the free energy of the host nematic^{6,7}. Colloidal ‘binding at a distance’ occurs when electrostatic and elastic forces balance each other at lower Z^*e , although this binding is weak and easily disrupted by thermal fluctuations (Fig. 1c, h).

Disks spontaneously rotate relative to \mathbf{n}_m with increasing temperature at $Z^*e \approx +(50–100)e$, with their orientations quantified by the polar and azimuthal angles θ and φ (Fig. 1b, Extended Data Fig. 1k). This reorientation arises from changing boundary conditions due to an interplay between electrostatic¹⁰ and temperature-dependent molecular interactions²⁷ at colloidal surfaces. Although chemically specific molecular (electrostatic) interactions favour orientations of 5CB molecules parallel (perpendicular) to disk surfaces, their competition yields narrow orientational distributions of disk normals ω_c relative to \mathbf{n}_m and an equilibrium polar angle $\theta = \theta_c$ at a given temperature (Fig. 1b, Extended Data Fig. 1g–l). The ‘corona’ of local disk-induced perturbations of orientational order preserves the $D_{\infty h}$ symmetry of disks and 5CB at $\omega_c \parallel \mathbf{n}_m$, but morphs to exhibit D_{2h} symmetry for $\omega_c \perp \mathbf{n}_m$ and C_{2h} symmetry for ω_c orientated obliquely to \mathbf{n}_m (Fig. 1f–m, Extended

Data Fig. 2, Supplementary Video 4). In dilute dispersions, thermal fluctuations freely rotate such disks around \mathbf{n}_m and the overall colloidal dispersion retains the uniaxial $D_{\infty h}$ symmetry of the 5CB nematic host (Extended Data Fig. 3a–c, Supplementary Video 1). Increasing the disk number density ρ leads to correlations of ω_c orientations, which can be controlled by an external magnetic field \mathbf{B} that aligns $\omega_c \perp \mathbf{B}$ (Extended Data Figs. 3, 4).

Low-symmetry nematic and smectic phases

The delicate interplay of anisotropic steric, electrostatic and elastic interactions is harnessed to obtain low-symmetry colloidal organizations that vary with temperature and both the charge and concentration of disks (Fig. 2, Extended Data Fig. 5a–j). The emergent orientational order of disks is characterized by a nonpolar colloidal director \mathbf{n}_c , a spontaneously selected average ω_c orientation. We observe a zoo of phases (Fig. 2), including nematic colloidal fluids with uniaxial, orthorhombic and monoclinic symmetries, as well as smectic and columnar phases that additionally feature positional correlations. Polarization-sensitive three-photon excitation fluorescence microscopy reveals that the ‘substrate’ LC host preserves a uniform far-field \mathbf{n}_m background at volume fractions of disks up to about 1.5% and

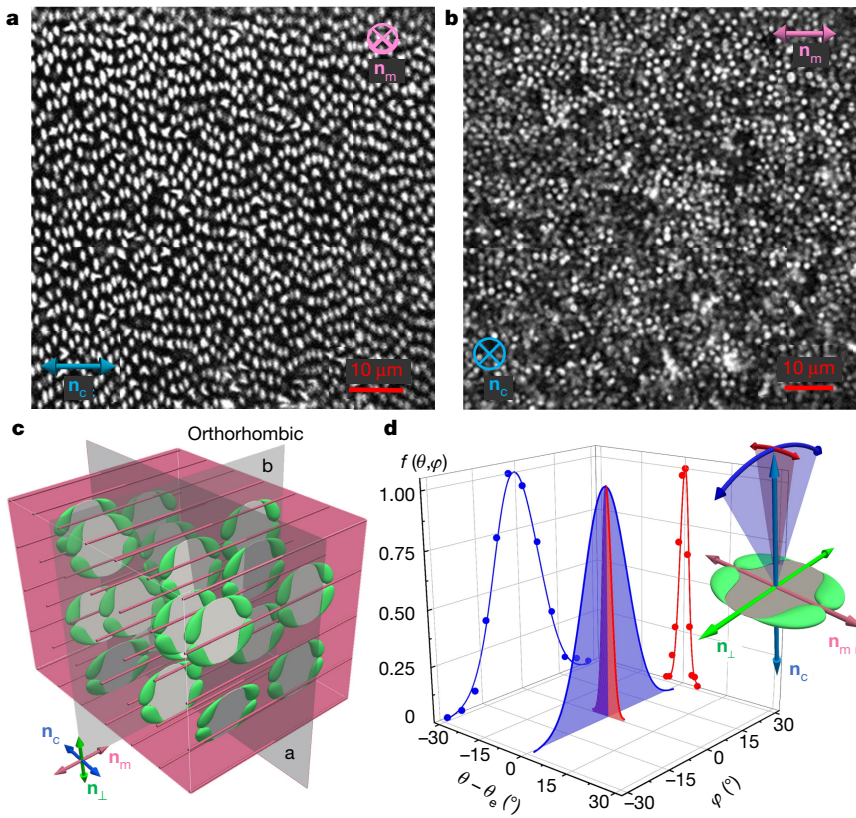


Fig. 3 | Colloidal orientational order within an orthorhombic nematic phase. **a, b,** Photon-upconverting luminescence confocal images of disks in the orthorhombic nematic samples at $T = 27.0 \pm 0.1^\circ\text{C}$ with $\rho = 0.34 \mu\text{m}^{-3}$ (**a**) and $\rho = 0.31 \mu\text{m}^{-3}$ (**b**) and with in-plane and out-of-plane $\mathbf{n}_c \perp \mathbf{n}_m$, respectively. **c,** The corresponding numerical visualization, with the confocal cross-sections shown by grey planes. **d,** $f_c(\theta, \varphi)$ versus polar $\theta - \theta_c$ (red curve) and azimuthal φ (blue curve) angles for the orthorhombic nematic state at $T = 27.0 \pm 0.1^\circ\text{C}$ and $\rho = 0.34 \mu\text{m}^{-3}$. The inset shows the directors and widths of the orientational distributions in the polar (red double arrow) and azimuthal (blue double arrow) directions relative to \mathbf{n}_m . The disk charge is $Z^*e \approx +80e$.

temperatures $\leq 34.6^\circ\text{C}$, with only weak perturbations of the order of the host nematic near the disk edges, irrespective of the phase symmetry (Extended Data Fig. 5k–n, Supplementary Video 5).

Direct 3D imaging reveals how low-symmetry phases arise with increasing ρ of freely diffusing nematic colloidal building blocks that comprise disks within an aligned 5CB host, with weakly perturbed local molecular order around disk edges (Figs. 3, 4, Extended Data Figs. 5–7, Supplementary Videos 2, 3). Orientational distribution functions $f_c(\omega_c)$, derived from image analysis, quantify orientational order through the uniaxial, biaxial and monoclinic order parameters, respectively given by:

$$\begin{aligned} S &= \int d\omega_c f_c(\omega_c) \mathcal{P}_2(\omega_c), \\ \Delta &= \int d\omega_c f_c(\omega_c) D_2(\omega_c), \\ M &= \sin(2\theta_{nc}), \end{aligned} \quad (1)$$

where $\mathcal{P}_2(\omega_c) = \frac{3}{2}\cos^2\theta - \frac{1}{2}$, $D_2(\omega_c) = \sin^2\theta\cos(2\varphi)$ and θ_{nc} is the angle between \mathbf{n}_c and \mathbf{n}_m . In an orthorhombic D_{2h} nematic, one finds $\mathbf{n}_c \perp \mathbf{n}_m$ in samples with both out-of-plane and in-plane \mathbf{n}_m (Fig. 3a–c), with narrow 4° – 8° polar and broader 15° – 30° azimuthal widths of $f_c(\theta, \varphi)$ (Fig. 3d). For the monoclinic C_{2h} nematic, \mathbf{n}_c and \mathbf{n}_m orient obliquely to each other (Fig. 4a–e). Azimuthal distributions $f_c(\varphi)$ broaden with increasing temperature and become narrower with increasing ρ , driving the corresponding variations of Δ (Fig. 4f, Extended Data Fig. 6j–l). As the polar distributions $f_c(\theta)$ morph and shift with temperature and \mathbf{n}_c rotates relative to \mathbf{n}_m (Fig. 4g), S varies from about -0.5 to about 1 when the system transitions between orthorhombic D_{2h} , monoclinic C_{2h} and uniaxial $D_{\infty h}$ states, before dropping to $S = 0$ at the transition to the high-temperature isotropic phase (Fig. 4e). The corresponding Δ changes from $\Delta \approx 1$ to $\Delta = 0$ with increasing temperature, whereas the geometric monoclinicity parameter is $M = 0$ in both the uniaxial and orthorhombic limits, but is non-zero in the monoclinic phase (Fig. 4e).

The monoclinic $f_c(\theta, \varphi)$ has only one mirror-symmetry plane at $\varphi = 0$ (Fig. 4h) and features a skewed distribution in θ , with fluctuations of the polar disk orientations about the equilibrium θ_{nc} being fundamentally asymmetric. The monoclinic nature of the nematic state is manifested not only by the oblique orientation of \mathbf{n}_c and \mathbf{n}_m , but also at the level of colloidal order alone (Fig. 4h). $S \neq 0$ and $\Delta \neq 0$ reflect the presence of different aligning directions, whereas geometric monoclinicity $M \neq 0$ and the skewness of $f_c(\theta, \varphi)$ reveal orientational monoclinic order. Whereas monoclinic and orthorhombic crystals reflect symmetries of the underlying crystallographic lattices, our lattice-free nematic colloids can exhibit such symmetries at the level of orientational fluid order alone. The frame of the orthorhombic nematic (Fig. 3a–d) is spanned by the π -rotation symmetry axes, $\mathbf{n}_m \perp \mathbf{n}_c \perp \mathbf{n}_\perp$, where pairs of these directors define the system's mirror-symmetry planes. The monoclinic nematic, however, has only one π -rotation axis, \mathbf{n}_\perp , which is orthogonal to a single mirror-symmetry plane containing \mathbf{n}_m and \mathbf{n}_c (Fig. 4). Fourier analysis of pairwise disk separation vectors reveals how these symmetries of orientational order co-exist with uninhibited fluidity, without positional correlations (Fig. 2b, c, Extended Data Fig. 7). Nevertheless, pretransitional local smectic correlations emerge near the smectic phase and remotely resemble cybotaxic molecular clusters in conventional LCs (Supplementary Video 3)^{1,2}.

At $Z^*e \approx +(50-100)e$ and room temperature, increasing ρ drives a uniaxial–orthorhombic nematic transition when the normals ω_c self-organize along $\mathbf{n}_c \perp \mathbf{n}_m$ (Figs. 2a, b, 3a–d). Increasing ρ at elevated temperatures of 30 – 33.5°C instead leads to a transition from the uniaxial nematic to the monoclinic nematic and smectic phases, each with C_{2h} symmetry (Figs. 2a, c, d, 4, 5a–d). Increasing the temperature at $\rho \geq 0.3 \mu\text{m}^{-3}$ transforms the orthorhombic nematic (Figs. 2a, 3a–d, Supplementary Video 2) into a lower-symmetry monoclinic C_{2h} nematic (Fig. 4, Supplementary Video 3) and subsequently into a C_{2h} smectic (Fig. 5a–d, Supplementary Video 6), followed by a re-entrant monoclinic C_{2h} nematic and a hybrid molecular–colloidal $D_{\infty h}$ uniaxial nematic, before crossing over into either an isotropic phase or

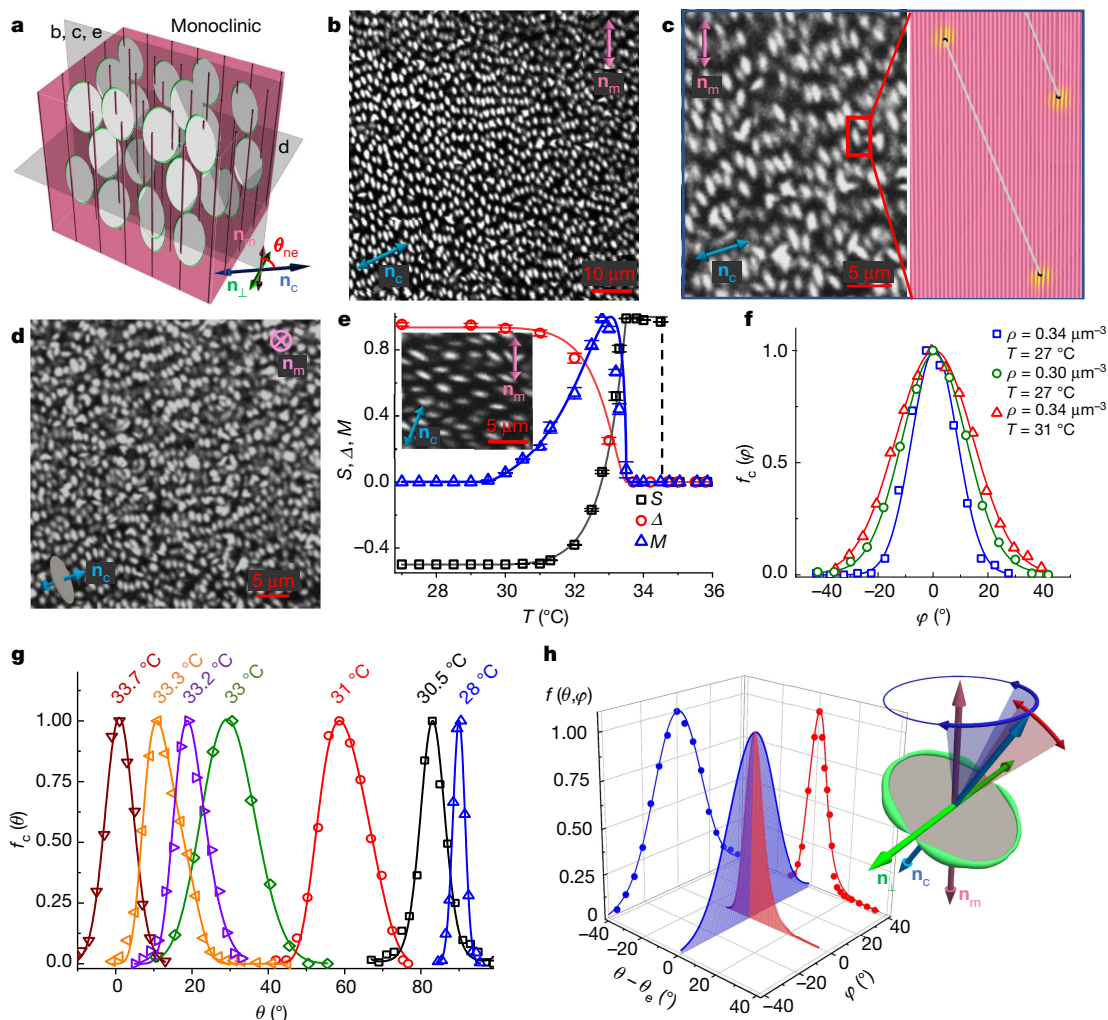


Fig. 4 | Colloidal orientational order within a monoclinic nematic phase. **a–d**, Numerical visualization (**a**) and confocal cross-sectional images (**b–d**) showing disk and \mathbf{n}_c orientations relative to \mathbf{n}_m in the monoclinic nematic phase at $\rho = 0.31 \mu\text{m}^{-3}$ and at $\theta_{ne} = 65^\circ \pm 2^\circ$ (**b**), $\theta_{ne} = 72^\circ \pm 2^\circ$ (**c**) and $\theta_{ne} = 32^\circ \pm 2^\circ$ (**d**). The inset in **c** shows a uniform \mathbf{n}_m in between disks at experimental distances, as obtained from Landau–de Gennes modelling, with weak distortions only at disk edges (shown in yellow). **e**, Δ , S and M versus T during system transitions between different phases with and without smectic correlations (Fig. 2a). Unless smaller than the symbols, error bars based on experimental angle measurements (Methods) are shown. Theoretical solid curves given by equation (1) based on measured θ_c values match experimental data without any adjustable parameters. The inset in **e** is a confocal micrograph of the

uniaxial colloidal nematic state (Extended Data Figs. 3k, l, 5h–j, Supplementary Video 7), depending on ρ . Conventional phase transitions with increasing temperature tend to melt ordered states in stages towards full disorder^{1,2}. By contrast, we observe formation of more ordered, lower-symmetry monoclinic nematic (including re-entrant) and smectic states upon heating the orthorhombic nematic LC (Fig. 2). Such ‘freezing by heating’²⁸ emerges within an equilibrium setting from the symmetry breaking prompted by changes of LC–colloidal surface coupling and the ensuing interplay of elastic, electrostatic and steric interactions. When ω_c resides on a θ_c cone relative to \mathbf{n}_m ($0 < \theta_c < \pi/2$), the threshold for the transition from the uniaxial to the orthorhombic or monoclinic state with increasing ρ also decreases (Fig. 2a) because disks access fewer orientational states compared to the $\omega_c \perp \mathbf{n}_m$ case. Elastic interactions in the vicinity of $\theta_c \approx \pi/4$ stabilize a C_{2h} smectic LC featuring one-dimensional positional order of disks that freely move within layers, with the nearest-neighbour distances

monoclinic nematic state with $\theta_{ne} = 20^\circ \pm 2^\circ$ at $\rho = 0.31 \mu\text{m}^{-3}$ and $T = 33.2 \pm 0.1^\circ\text{C}$. **f**, $f_c(\theta, \varphi)$ versus φ at different T and ρ values. **g**, $f_c(\theta, \varphi)$ versus θ at $\rho = 0.28 \mu\text{m}^{-3}$ and different T values. **h**, $f_c(\theta, \varphi)$ versus $\theta - \theta_c$ (red curve) and φ (blue curve) describing disk orientations in a monoclinic nematic at $T = 33.3 \pm 0.1^\circ\text{C}$ and $\rho = 0.28 \mu\text{m}^{-3}$, obtained by fitting experimental data (red/blue symbols) with $f_c(\theta, \varphi) \propto \exp\left[\frac{5}{4}cSP_2(\omega_c) + \frac{15}{16}c\Delta D_2(\omega_c) - \varepsilon_2(\theta - \theta_c)^2 - \varepsilon_3(\theta - \theta_c)^3 - \varepsilon_4(\theta - \theta_c)^4\right]$ using experimental Δ and S (Supplementary Information); the fitting parameters are $\varepsilon_2 = 88 \pm 6$, $\varepsilon_3 = -550 \pm 54$ and $\varepsilon_4 = 1,608 \pm 308$. The inset in **h** schematically shows the widths of the orientational distributions in the polar (red) and azimuthal (blue) directions; note the skewness in the polar angle plane. The disk charge is $Z^*e = +80e$.

r_{sm} being smaller than the layer spacing σ_{sm} (Fig. 5a–d, Supplementary Video 6).

Thermal and magnetic reconfiguration of order

The temperature-dependent interplay between various colloidal interactions allows real-time reversible thermal reconfiguration of assemblies. As an example, Supplementary Video 8 shows how the out-of-equilibrium transformation of a D_{2h} orthorhombic into a C_{2h} monoclinic nematic state is followed by the formation and subsequent dissociation of smectic colloidal layers with C_{2h} symmetry upon a modest temperature change of about 5°C , all within about 15 min. This reconfiguration is enriched by our system’s facile response to external fields. For example, by exploiting the magnetic response of disks, which tends to orient $\omega_c \perp \mathbf{B}$, we show that the \mathbf{n}_c of the smectic can be rotated by a 100-mT field from its original orientation within layers to

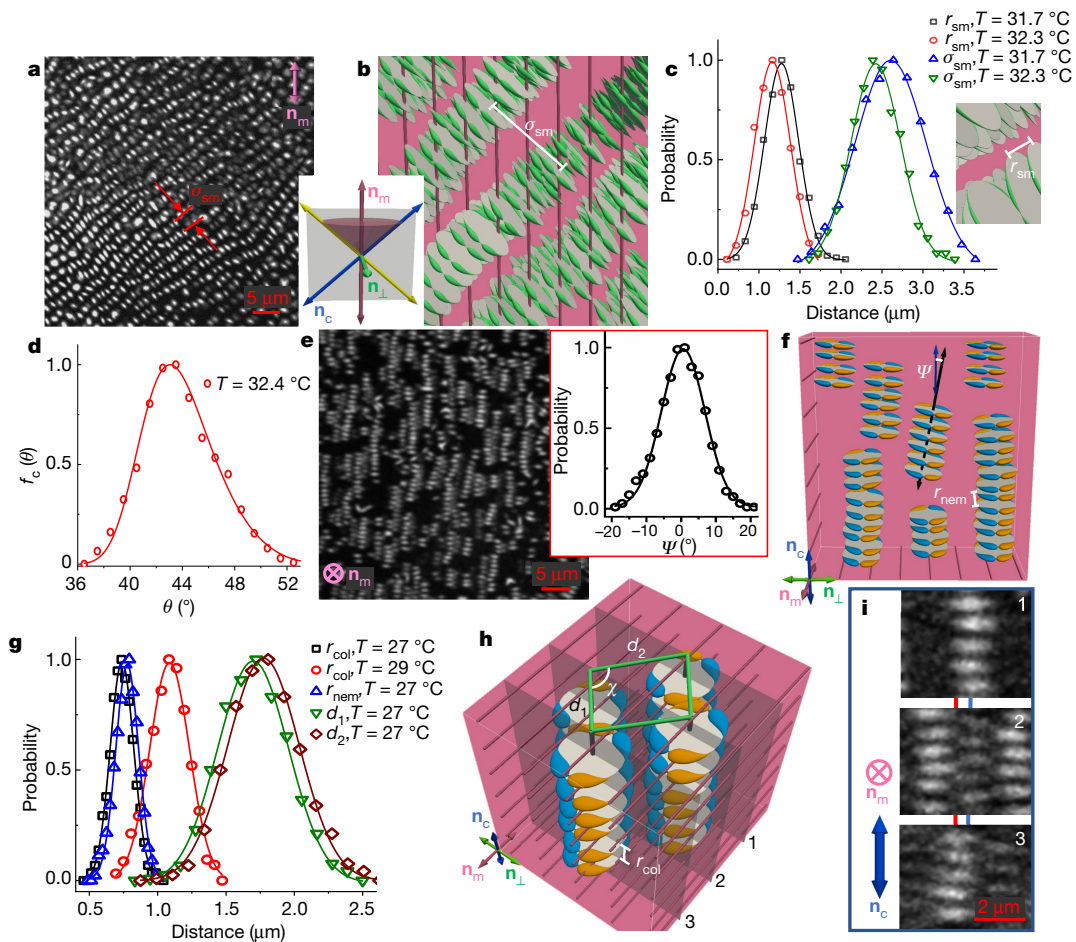


Fig. 5 | Order within monoclinic smectic and columnar states.

a, b, Photon-up-converting luminescence confocal image (**a**) and numerical visualization (**b**) in the monoclinic smectic state at $\rho = 0.29 \mu\text{m}^{-3}$ and $T = 31.7 \pm 0.1 \text{ }^\circ\text{C}$. **c**, The corresponding distributions of the centre-to-centre distance r_{sm} and smectic layer spacing σ_{sm} at different T values. **d**, $f_c(\theta)$ in the monoclinic smectic state. **e, f**, Confocal micrographs (**e**) and numerical visualization (**f**) of an orthorhombic columnar nematic at $\rho = 0.23 \mu\text{m}^{-3}$ and $T = 27.0 \pm 0.1 \text{ }^\circ\text{C}$. The right-side inset in **e** shows the probability distribution of angles ψ between individual columns and \mathbf{n}_c , as defined in **f, g**. Distributions of centre-to-centre distances r_{nem} in the orthorhombic columnar nematic (**f**) and r_{col} and columnar lattice parameters d_1 and d_2 in the columnar phase (**h**) at different T values. **h**, 3D rendering of a columnar oblique primitive cell based

on confocal imaging of disks, depicted along with the definitions of the geometric parameters d_1 , d_2 , r_{col} , and χ of the cell, which characterize the colloidal columnar order. **i**, Confocal cross-sections of the columnar phase within the planes labelled in **h**, showing edge-on disks away from the confining glass surface at depths of $1.00 \pm 0.05 \mu\text{m}$, $3.00 \pm 0.05 \mu\text{m}$ and $5.00 \pm 0.05 \mu\text{m}$. Red and blue lines beneath the confocal slices highlight the slight shift of column centres within the cross-sectional scans, consistent with the 3D rendering in **h**; $\rho = 0.32 \mu\text{m}^{-3}$ and $T = 27.0 \pm 0.1 \text{ }^\circ\text{C}$. Measurement errors are less than $\pm 50 \text{ nm}$ for r_{sm} , σ_{sm} , r_{nem} , d_1 , d_2 , r_{col} , and $\pm 1^\circ$ for ψ and χ ; broad distributions reflect the intrinsic spatial variation of these parameters (Methods). Disk charges are $Z^*e \approx +80e$ (**a–d**) and $Z^*e \approx +20e$ (**e–i**).

make an oblique angle with the plane containing the layer normal and \mathbf{n}_m , thus yielding a C_{2h} symmetry (Extended Data Fig. 8, Supplementary Video 6). This triclinic smectic structure^{2,23,24} has no symmetry operations other than trivial ones and is induced at merely 100 mT, which would have negligible effects on conventional LCs, demonstrating how the molecular–colloidal organizations can be exquisitely controlled by external fields.

Phases with columnar positional correlations

At $Z^*e < +50e$, the electrostatic double-layer torques¹⁰ are insufficiently strong to rotate disks away from $\omega_c \perp \mathbf{n}_m$ with increasing temperature. The interplay of the weakened repulsive electrostatic with anisotropic elastic interactions favours column-like assemblies²⁹ within 5CB (Fig. 2a, Extended Data Figs. 5g, j, 9a–c). The columns resemble molecular stacks of chromonic LCs³⁰ but are comprised of well separated disks, instead of molecular aggregates, that arise from competing electrostatic and elastic interactions, as demonstrated for colloidal dimers in Fig. 1c, h. With increasing ρ , an orthorhombic D_{2h} columnar nematic state emerges,

which exhibits a narrow distribution of columnar orientations with $\mathbf{n}_c \perp \mathbf{n}_m$ (Fig. 5e, f, Supplementary Video 9). At even higher ρ , a columnar state appears (Fig. 5g–i, Extended Data Figs. 5d, 9d–g), featuring a two-dimensional locally monoclinic (oblique) lattice²⁹ of colloidal columns immersed within a molecular nematic host with $\mathbf{n}_c \perp \mathbf{n}_m$. This colloidal organization has a π -rotation symmetry axis of the oblique lattice along the columns and (orthogonal to it) a mirror-symmetry plane containing the oblique primitive cell and disks²⁹. The inter-particle distance r_{col} within columns and the inter-columnar distances $d_1 \neq d_2$ within the elementary cell, extracted from the 3D images, vary with temperature (Fig. 5g–i). The orientational and positional distributions of disks are relatively broad (Fig. 5g–i, Extended Data Fig. 9d–g). Because the difference between the lattice parameters $d_1 \neq d_2$ is small and the columnar symmetry would be orthorhombic for $d_1 = d_2$, an open question remains of whether the locally monoclinic columnar structure is an intrinsic bulk property of our system or it is possibly induced by confinement and finite-system-size effects. Upon increasing the temperature, columnar lattices melt and the columns themselves eventually dissociate (Extended Data Fig. 9h–k). Depending on ρ , this leads to

reversible transitions to uniaxial or orthorhombic nematics comprised of individual disks, before crossing over to isotropic or uniaxial colloidal nematic states at $T \geq 34.7^\circ\text{C}$ (Fig. 2a, Supplementary Video 10).

Discussion and conclusions

The phase and ordering behaviours of our system are captured by analytical modelling of key interactions at molecular and colloidal scales. Starting from the Onsager–Parsons theory (Supplementary Information)¹, suitably adapted to include higher-order electrostatics-enriched particle correlations along with surface boundary conditions and elastic forces, we scrutinize the phase behaviour of disks in a molecular LC host. The emerging diagram distinctly features uniaxial, orthorhombic and monoclinic nematic phases at $Z^*e = +80e$ and the predicted order parameters agree with experiments (Figs. 2a, e, 4e). A simple bifurcation analysis shows how the elastic interactions between disks drive a nematic–smectic transition within a central fraction of the temperature range of monoclinic order when the quadrupolar elastic forces are strongly attractive for a colloidal centre-to-centre separation vector at about 45° relative to \mathbf{n}_m , in agreement with experiments (Fig. 2a, e, Extended Data Fig. 10). Computer simulations of energy-minimizing \mathbf{n}_m distortions around disks at experimentally determined orientations and positions explain how lattices of colloidal columns emerge (Fig. 5g–i, Extended Data Fig. 9d–g) when quadrupolar-like elastic interactions between disks balance the anisotropic electrostatic repulsions, with regions of locally distorted \mathbf{n}_m maximally overlapping while keeping like-charged disk surfaces apart.

Remarkably, the highly sought-after monoclinic nematic^{12–15}, smectic^{1,2} and columnar²⁹ states all exist within a single system of two building blocks, both having uniaxial symmetry. The emergent low-symmetry order arises from a thermal self-reconfiguration of relative orientations of the molecular and colloidal subsystems, supplemented with competing anisotropic elastic, steric and electrostatic colloidal interactions. Our approach could be extended to generate other mesophases by choosing different LC hosts and colloidal particles with various shapes carrying magnetic or electrostatic dipoles. For example, colloidal particles with C_{2h} symmetry could form triclinic C_{1h} nematics under conditions when the surface-interaction-controlled ordering axes of the particles are different from the principal director of the nematic host. Such strategies could impart designable ferroelectric, ferromagnetic, piezoelectric and other properties on the ensuing materials. Unlike in solids, where symmetries of the crystal basis are required to be compatible with crystallographic lattices, no such constraints apply to nematic fluids, which can therefore adopt a larger variety of symmetries yet to be discovered^{1,2}. The inventory of self-assembled colloidal crystals is still much smaller than that of their atomic counterparts, which are abundantly found in nature⁹, with the colloidal cubic diamond having been reported only recently³¹. By contrast, our nematic colloids with shape- and size-dissimilar building blocks exhibit a wealth of fluid phases, such as monoclinic nematics, that exceed what has been found in nature so far and may inspire the quest for similar condensed matter states in molecular, polymeric, micellar and other systems.

To conclude, we have developed a soft-matter system that exhibits orientational fluid order with the lowest monoclinic symmetry demonstrated so far, which emerges from the oblique mutual self-alignment of uniaxial colloidal and molecular building blocks at the mesoscale. Monoclinic order is unambiguously revealed through the direct imaging of disks that exhibit a skewed orientational distribution and by the oblique relative alignment of the molecular and colloidal directors. Although many solid substances, such as the common painkiller paracetamol³², can inter-transform between monoclinic and orthorhombic states, our work demonstrates that the plurality of low

symmetries of orientational order can also be achieved in colloidal LC fluids. Low-symmetry nematic, smectic and columnar states of LC colloids may find important uses in applications ranging from displays to biodetectors and studies of non-Abelian topological defects near orthorhombic–monoclinic nematic transitions¹⁵.

Online content

Any methods, additional references, Nature Research reporting summaries, source data, extended data, supplementary information, acknowledgements, peer review information; details of author contributions and competing interests; and statements of data and code availability are available at <https://doi.org/10.1038/s41586-021-03249-0>.

- Chaikin, P. M. & Lubensky, T. C. *Principles of Condensed Matter Physics* (Cambridge Univ. Press, 1995).
- de Gennes, P. G. & Prost, J. *The Physics of Liquid Crystals* 2nd edn (Clarendon Press, 1993).
- Alben, R. Liquid crystal phase transitions in mixtures of rodlike and platelike molecules. *J. Chem. Phys.* **59**, 4299–4304 (1973).
- van der Koij, F. M. & Lekkerkerker, H. N. W. Liquid-crystal phases formed in mixed suspensions of rod- and platelike colloids. *Langmuir* **16**, 10144–10149 (2000).
- Berardi, R. & Zannoni, C. Low-temperature biaxial nematic from rod and disc mesogen mixture. *Soft Matter* **8**, 2017–2025 (2012).
- Poulin, P., Stark, H., Lubensky, T. C. & Weitz, D. A. Novel colloidal interactions in anisotropic fluids. *Science* **275**, 1770–1773 (1997).
- Mušević, I., Škarabot, M., Tkalec, U., Ravnik, M. & Žumer, S. Two-dimensional nematic colloidal crystals self-assembled by topological defects. *Science* **313**, 954–958 (2006).
- Silvestre, N. M., Patricio, P., Tassinkevych, M., Andrienko, D. & Telo da Gama, M. M. Colloidal discs in nematic liquid crystals. *J. Phys. Condens. Matter* **16**, S1921–S1930 (2004).
- Smalyukh, I. I. Liquid crystal colloids. *Annu. Rev. Condens. Matter Phys.* **9**, 207–226 (2018).
- Mundoor, H. et al. Electrostatically controlled surface boundary conditions in nematic liquid crystals and colloids. *Sci. Adv.* **5**, eaax4257 (2019).
- Mertelj, A., Lisjak, D., Drofenik, M. & Čopič, M. Ferromagnetism in suspensions of magnetic platelets in liquid crystal. *Nature* **504**, 237–241 (2013).
- Lubensky, T. C. & Radzihovsky, L. Theory of bent-core liquid-crystal phases and phase transitions. *Phys. Rev. E* **66**, 031704 (2002).
- Luckhurst, G. R., Naemura, S., Sluckin, T. J., To, T. B. T. & Turzi, S. Molecular field theory for biaxial nematic liquid crystals composed of molecules with C_{2v} point group symmetry. *Phys. Rev. E* **84**, 011704 (2011).
- Mettout, B. Macroscopic and molecular symmetries of unconventional nematic phases. *Phys. Rev. E* **74**, 041701 (2006).
- Luckhurst, G. R. & Sluckin, T. J. *Biaxial Nematic Liquid Crystals: Theory, Simulation and Experiment* (Wiley, 2015).
- Liu, Q., Ackerman, P. J., Lubensky, T. C. & Smalyukh, I. I. Biaxial ferromagnetic liquid crystal colloids. *Proc. Natl Acad. Sci. USA* **113**, 10479–10484 (2016).
- Freiser, M. J. Ordered states of a nematic liquid. *Phys. Rev. Lett.* **24**, 1041–1043 (1970).
- Yu, L. J. & Saupé, A. Observation of a biaxial nematic phase in potassium laurate-1-decanol-water mixtures. *Phys. Rev. Lett.* **45**, 1000–1003 (1980).
- Severing, K. & Saalwächter, K. Biaxial nematic phase in a thermotropic liquid-crystalline side-chain polymer. *Phys. Rev. Lett.* **92**, 125501 (2004).
- van den Pol, E., Petukhov, A. V., Thies-Weesie, D. M. E., Byelov, D. V. & Vroege, G. J. Experimental realization of biaxial liquid crystal phases in colloidal dispersions of boardlike particles. *Phys. Rev. Lett.* **103**, 258301 (2009).
- Mundoor, H., Park, S., Senyuk, B., Wensink, H. H. & Smalyukh, I. I. Hybrid molecular-colloidal liquid crystals. *Science* **360**, 768–771 (2018).
- Cladis, P. E. New liquid-crystal phase diagram. *Phys. Rev. Lett.* **35**, 48–51 (1975).
- Jákli, A., Krüerke, D., Sawade, H. & Heppke, G. Evidence for triclinic symmetry in smectic liquid crystals of bent-shape molecules. *Phys. Rev. Lett.* **86**, 5715–5718 (2001).
- Vaupotič, N. et al. Evidence for general tilt columnar liquid crystalline phase. *Soft Matter* **5**, 2281–2285 (2009).
- Yang, J. et al. One-step hydrothermal synthesis of carboxyl-functionalised upconversion phosphors for bioapplications. *Chemistry* **18**, 13642–13650 (2012).
- Graf, C., Vossen, D. L. J., Imhof, A. & van Blaaderen, A. A. General method to coat colloidal particles with silica. *Langmuir* **19**, 6693–6700 (2003).
- Jérôme, B. Surface effects and anchoring in liquid crystals. *Rep. Prog. Phys.* **54**, 391 (1991).
- Helbing, D., Farkas, I. J. & Viscek, T. Freezing by heating in a driven mesoscopic system. *Phys. Rev. Lett.* **84**, 1240–1243 (2000).
- Mamlok, L., Malthe, J., Tinh, N. H., Destradre, C. & Levelut, A. M. Une nouvelle mésophase en colonnes. *J. Phys. Lett.* **43**, 641–647 (1982).
- Lydon, J. Chromonic review. *J. Mater. Chem.* **20**, 10071–10099 (2010).
- He, M. et al. Colloidal diamond. *Nature* **585**, 524–529 (2020).
- Moynihan, H. A. & O'Hare, I. P. Spectroscopic characterisation of the monoclinic and orthorhombic forms of paracetamol. *Int. J. Pharm.* **247**, 179–185 (2002).

Publisher's note Springer Nature remains neutral with regard to jurisdictional claims in published maps and institutional affiliations.

© The Author(s), under exclusive licence to Springer Nature Limited 2021

Methods

Preparation of colloidal disks

Disk-shaped β -NaYF₄:Yb/Er particles, designed to exhibit upconversion luminescence when excited at 980 nm, were synthesized following the hydrothermal synthesis method^{10,25}. Precursors and solvents used for the synthesis were of analytical grade and used without additional purifications. We purchased ytterbium nitrate hexahydrate (Yb(NO₃)₃·6H₂O), yttrium nitrate hexahydrate (Y(NO₃)₃·6H₂O), erbium nitrate pentahydrate (Er(NO₃)₃·5H₂O), sodium fluoride and oxalic acid from Sigma Aldrich. Sodium hydroxide was purchased from Alfa Aesar. In a typical reaction, we dissolved 0.7 g of sodium hydroxide in 10 ml of deionized water, and then 5 ml of oxalic acid solution (2 g, 19.2 mmol) in deionized water was added to the solution at room temperature to obtain a clear transparent solution. Subsequently, 5 ml of sodium fluoride solution (202 mg, 4.8 mmol) was added to the mixture under vigorous stirring that continued for 15 min. Then, we injected 1.1 ml of Y(NO₃)₃ (0.88 mmol), 0.35 ml of Yb(NO₃)₃ and 0.05 ml of Er(NO₃)₃ into the above solution under vigorous stirring. After stirring for another 20 min at room temperature, the mixture was transferred to a 40-ml Teflon chamber (Col-Int. Tech.) and heated at 200 °C for 12 h. After the reaction, the mixture was allowed to cool down to room temperature naturally, and the particles (precipitated at the bottom of the reaction chamber) were collected by centrifugation, washed with deionized water multiple times, and finally dispersed in 10 ml of deionized water. This synthesis method yields the 10-nm-thick disks shown in Fig. 1a.

Surface functionalization and electrostatic stabilization of disks

The disks were surface-functionalized with a thin layer of silica and polyethylene glycol (Extended Data Fig. 1b–e)^{10,16,26}. For this, 1 ml of colloidal dispersion in deionized water was mixed with 5 ml of hydrogen peroxide (H₂O₂), and then 100 μ l of nitric acid (HNO₃) was added dropwise into the solution and kept under vigorous mechanical agitation for 12 h. During this reaction, the disks acquired positive surface charges, while oxalic acid molecules attached to the surfaces of the particles were oxidized. The charged disks were precipitated from the solution by centrifugation and dispersed in 1 ml of ethanol. We then coated the surfaces of the particles with thin layers of silica. Briefly, 75 mg of polyvinyl pyrrolidone (molecular weight 40,000) was dissolved in 4 ml of ethanol and mixed with 1 ml of colloidal dispersion in ethanol. The solution was kept under continuous mechanical agitation for 24 h to ensure the adsorption of polyvinyl pyrrolidone on the colloidal surfaces. The particles were separated from the solution by centrifugation and redispersed in 5 ml of ethanol. Then, we added 200 μ l of ammonia solution and 6 μ l of tetraethyl orthosilicate (Sigma Aldrich) to the solution under vigorous mechanical agitation. After 12 h, the silica-coated disks were collected by centrifugation and washed with ethanol and deionized water and redispersed in 4 ml of ethanol. The solution pH was adjusted to 12 by adding ammonia solution (28% in water). Then, we dissolved 35 mg of silane-terminated polyethylene glycol (molecular weight 5,000) in 1 ml of ethanol at 50 °C and mixed with the colloidal dispersions of the silica-capped particles and kept at 35 °C under continuous mechanical agitation. After 12 h, the surface-functionalized disks were collected by centrifugation, washed with ethanol and water, and finally dispersed in 1 ml of ethanol. Although the process of silica capping tends to reduce the positive charge of disks, the effective charge remains positive at +(100–150)*e* for the ≤ 5 nm silica thickness used in our experiments. The surface charge of the disks below +100*e* was tuned by controlled ageing of their dispersion in ethanol. The positive charge resides on the NaYF₄ core of the as-synthesized and surface-functionalized disks.

Video microscopy, laser trapping and characterization of colloidal charge

A charge-coupled device camera (Flea-COL, from Point Grey Research) mounted on upright BX-51 or inverted IX-71 microscopes (both from

Olympus) was used for bright-field transmission-mode optical imaging and video microscopy. Olympus objectives with 10–100 \times magnifications and numerical apertures of 0.2–1.4 were used in this imaging and video recording. The microscopes were additionally equipped with pairs of crossed linear polarizers and 530-nm phase-retardation plates for the polarizing optical microscopy experiments. A holographic laser tweezer system coupled to the optical microscopes was used to probe colloidal interactions between particles by bringing them close to each other and releasing them from the laser traps^{33–35}.

The surface charge of the colloidal disks was characterized by probing their electrophoretic motions within 5CB when subjected to an external d.c. electric field E_{DC} (ref. 10). LC cells for these measurements were prepared by sandwiching two polyvinyl alcohol-coated glass plates with a spacing of about 30 μ m, set using strips of aluminium foil that also served as electrodes. The electrodes were connected to an external d.c. source (DS340, Stanford Research Systems) by copper wires. A dilute dispersion of disks in 5CB was infiltrated to the cell by means of capillary forces. A d.c. voltage of 5 V was applied between the electrodes, and the particle displacement was video-recorded (Extended Data Fig. 1m). Disk velocities v_D were obtained by measuring their displacements extracted from the video frames (with a measurement error of ± 10 nm) in a selected time interval (Extended Data Fig. 1n) using the image-processing software ImageJ (version 1.52a, freeware from the National Institute of Health)³³. The effective surface charge of the colloidal disks was estimated from the highly overdamped motion reflecting a balance of viscous drag and electrostatic forces acting on the disks, $\eta_f v_D = Z^* e E_{DC}$, where the d.c. electric field magnitude E_{DC} was calculated using the inter-electrode distance and applied voltage¹⁰. The frictional coefficient was determined as $\eta_f = k_B T / D_f$, where k_B and D_f are the Boltzmann and diffusion constants, respectively^{10,33,34}. The diffusion constant D_f of the particles was estimated based on the Brownian motion of the particle within the same 5CB host^{33,34} using the distribution of particle displacements recorded at a rate of 15 frames per second (Extended Data Fig. 1o)^{10,33–35}. The relative errors for measuring η_f , $Z^* e$ and D_f were $\pm 0.5\%$, $\pm 1\%$ and $\pm 0.5\%$, respectively.

Nematic colloidal particle dispersion and self-alignment

The polyethylene-glycol-functionalized disks were dispersed in 5CB (also known as pentylcyanobiphenyl and 4-cyano-4'-pentylbiphenyl, obtained from Frinton Labs) with a chemical structure shown in the inset of Extended Data Fig. 1a. Briefly, 20 μ l of disk dispersion in ethanol was mixed with 20 μ l of 5CB, followed by solvent evaporation at 75 °C for 2 h and quenching to room temperature under vigorous mechanical agitation, yielding well dispersed particles in the nematic host^{36–38}. The angle θ_e between \mathbf{n}_m and the disk normal ω_e varied within 0°–90°, depending on the temperature and the disk surface charge. At room temperature, disks with $> +200e$ ($< +100e$) surface charge exhibited orientations with $\theta_e = 0^\circ$ ($\theta_e = 90^\circ$), whereas conical alignment was observed for moderate surface charges $+(100–200)e$. For $+(50–100)e$, θ_e varied with the temperature (Fig. 1b, Extended Data Fig. 1j) and the ionic content of the LC host medium^{10,39}. Ageing dispersions of disks in as-purchased 5CB kept in an open bottle under ambient conditions for a few days to one week absorbed ions from the atmosphere, enabling control of the ionic content. The Debye screening length estimated for such samples¹⁰ was in the range $\xi_D = 0.1–0.5$ μ m, with the largest ξ_D found in freshly prepared samples with as-purchased 5CB.

Imaging and analysis of disk positions, orientations and order parameters

Optical imaging was performed using a multimodal 3D nonlinear imaging system built around a confocal system FV300 (from Olympus) and an inverted microscope (Olympus IX-81)^{37,40}. We used a 100 \times objective with a numerical aperture of 1.4 (Olympus UPlanFL) and a 980-nm pulsed output from a Ti:Sapphire oscillator (80 MHz, Coherent,

Chameleon ultra) to optically excite our colloidal photon-upconverting disks^{37,41}. To achieve point-by-point scanning, the laser beam was sent through a set of Galvano mirrors. To enable depth-resolved 3D imaging, the objective was mounted on a stepper motor capable of re-positioning the focal plane across the sample depth with nanometre precision. Luminescence signals from the disks (Extended Data Fig. 1f) were epi-collected by the same objective that was used for excitation; they were sent through a pinhole (confocal with the focal plane of the objective) before being detected by a photomultiplier tube, with additional filters introduced to block the high-intensity excitation beam. An objective heater (from Bioprotechs) mounted on the illumination objective was used to heat the sample for the temperature-dependent measurements, with a temperature control error less than ± 0.1 °C. Confocal photon-upconverting luminescence microscopy characterized the orientations, positions, order parameters and number density ρ of disks within different phases²¹. The orientations of the disk normal \mathbf{n}_c relative to \mathbf{n}_m were probed by analysing optical micrographs with the ImageJ software. Using samples with different experimental geometries and imaging planes either parallel or perpendicular to \mathbf{n}_m , we probed the polar θ and azimuthal φ angles of individual disks and then quantified the normalized orientational probabilities by $f_c(\theta, \varphi)$. By directly measuring the disk orientation angles θ and φ , the order parameters S and Δ were characterized in the orthorhombic and monoclinic phases, along with M in the monoclinic nematic state; only S was non-zero in the uniaxial phase. While S , Δ and M uniquely distinguish the isotropic fluid state of our system (where these three parameters are all equal to zero) from the anisotropic fluid states with nematic uniaxial, orthorhombic and monoclinic types of order, we also characterize these order parameters for the monoclinic smectic state, where low-symmetry orientational order co-exists with one-dimensional quasi-long-range positional order (Fig. 4e).

To directly characterize the spatial positions and orientations of the disks, we used samples with different geometries of orientations of \mathbf{n}_m and \mathbf{n}_c relative to the microscope's optical axis and sample and imaging planes, much like specially cut slabs with different orientations of crystallographic axes are used in studies of the physical properties of solid crystals⁴². Having \mathbf{n}_m and/or \mathbf{n}_c co-planar with the image planes was instrumental for the characterization of the orientational order parameters. Using particles with different orientations immobilized on surfaces and at different depths of the LC, we determined the error of measuring polar and azimuthal angles of individual disks with ImageJ to be $\pm(1^\circ-2^\circ)$ and the spatial centre-of-mass positions to be $\pm(10-50)$ nm, both varying with the imaging depth (determined as widths of Gaussian fits to the respective angular and positional distributions). The relative error of estimating the number density ρ based on counting disks within a volume of the 3D confocal images is 5%. Although confocal microscopy is a standard technique used in structural studies of colloidal crystals, glasses and LCs^{21,31,43-48}, our approach additionally takes advantage of the nonlinear photon-upconverting process that yields strong luminescence uniquely emitted by the disks⁴⁹, which was instrumental for resolving individual particles within the studied mesophases with the optical contrast appropriate for the image analysis that we performed.

Three-photon excitation fluorescence polarizing microscopy (3PEFPM) and corresponding spectral nonlinear optical fluorescence measurements were performed with the same microscope setup as described above, but using a 870-nm pulsed output from the tunable Ti:sapphire oscillator for exciting the 5CB molecules through a three-photon absorption process⁵⁰. The emission from the sample was collected in epi-detection mode and characterized using a spectrometer (USB 2000, Ocean Optics). A half-wave plate was introduced before the objective to rotate the polarization of the excitation beam⁵⁰. The absorption efficiency of the 5CB molecules and the ensuing fluorescence signal both depend strongly on the \mathbf{n}_m orientations relative to the polarization of the excitation beam (Extended Data Fig. 1a)^{21,50}.

We measured a series of fluorescence spectra while rotating the linear excitation polarization direction with respect to \mathbf{n}_m (Extended Data Figs. 1a, 5l) for the 5CB samples with the in-plane \mathbf{n}_m , confirming that the fluorescence intensity scales as $\cos^6\Omega_{3\text{PEFPM}}$, where $\Omega_{3\text{PEFPM}}$ is the angle between the polarization of the excitation light and \mathbf{n}_m , whereas the intensity remains at a minimum in cells with a vertical \mathbf{n}_m . Because the disks are very thin, the 3PEFPM images obtained using this fluorescence from 5CB in planar and homeotropic cells with disks at different concentrations up to $\sim 1.5\%$ by volume remain uniform throughout the samples (Extended Data Fig. 5k), indicating that the thin disks only locally and very minimally perturb \mathbf{n}_m while retaining its far-field background. The 3PEFPM intensity variation measured for the LC with disks shows a slightly different angular variation compared to pure 5CB with in-plane \mathbf{n}_m (Extended Data Fig. 5l), which is consistent with the nature of the orientational distribution of the molecules of the 5CB host with embedded disks (Extended Data Fig. 2, Supplementary Videos 4, 5). Given that the 3PEFPM signal originates directly from 5CB molecules, this indicates that the interaction of the molecular rods with the aligned colloidal disks perturbs the uniaxial distribution of molecular orientations at the disk edges, consistent with numerical modelling (Extended Data Fig. 2), although a detailed exploration of this effect is outside the scope of our present study.

Both upconversion-based confocal images of disks and 3PEFPM images of \mathbf{n}_m perturbations due to the disk presence are qualitatively similar when obtained at different sample depths of monodomain uniaxial, orthorhombic and monoclinic colloidal nematics. Unless specified differently, we provide them for sample depths 10–100 μm away from the confining surface that is closest to the imaging objective. The principal advantage of such 3D depth-resolved imaging of nematic colloids with translational invariance of the nematic phase symmetries is that it provides the ability to quantify the orientational order through direct imaging of individual disk orientations and positions (used to determine order parameters and orientational distributions), which is impossible to achieve with conventional fluorescence, bright-field or other microscopy techniques that lack 3D resolution (see comparisons in Supplementary Videos 1, 10). Differently, our 3D depth-resolved imaging of colloidal structures with positional ordering allows us to determine key characteristics of positional order, such as lattice parameters, in addition to probing the orientational order. Examples of such 3D images and reconstructed colloidal organizations based on them are provided in Fig. 5h, i, Extended Data Fig. 9d–g.

LC sample preparation and phase diagram

Dispersions of colloidal disks were infiltrated into glass cells with 10–100 μm gap thickness or rectangular capillaries (obtained from VitroCom) with 0.2×2.0 mm² or 0.5×5.0 mm² cross-sections using capillary forces. The gap thickness within the glass cell was set using Mylar films. Additionally, colloidal dispersions were filled into $2 \times 2 \times 3$ mm³ containers obtained by 3D-printing it (using a Lulzbot Taz 3D printer, purchased from Lulzbot) atop of a glass coverslip with a desired alignment layer for \mathbf{n}_m . For the studied ranges of ρ and T , no difference in phase behaviour was observed for samples of thickness ≥ 10 μm , regardless of the different types of confinement and sample preparation. To obtain monodomain samples with perpendicular boundary conditions for \mathbf{n}_m , the inner surfaces of cells, containers and capillaries were treated with surfactant dimethyloctadecyl[3-(trimethoxysilyl)propyl] ammonium chloride (obtained from Acros Organics). To achieve unidirectional planar surface boundary conditions for \mathbf{n}_m , the top and bottom substrates were coated with 1wt% aqueous polyvinyl alcohol (Sigma Aldrich) and rubbed to define the direction of \mathbf{n}_m . No surface treatment was used to control the boundary conditions for \mathbf{n}_c , so that we observed orthorhombic and monoclinic nematics with spontaneously monodomain and sometimes polydomain \mathbf{n}_c orientations within the studied fields of view (Supplementary Videos 2, 3). The phase diagram (Fig. 2a) was obtained by preparing a series of samples with different

colloidal disk charge and number density and then changing the temperature with a step of 0.1 °C while probing the colloidal behaviour after about 30 min of thermal equilibration at each temperature.

Data availability

Additional relevant data, such as details of the experimental phase diagram, are provided in the Supplementary Information. Additional raw data that further support the findings of this study are available from the corresponding author on reasonable request. Source data are provided with this paper.

Code availability

The custom codes used to generate plots and theoretical phase diagrams, as well as the Landau–de Gennes modelling and polarizing microscopy image simulation codes, are all provided in the Supplementary Information.

33. Senyuk, B., Glugla, D. & Smalyukh, I. I. Rotational and translational diffusion of anisotropic gold nanoparticles in liquid crystals controlled by varying surface anchoring. *Phys. Rev. E* **88**, 062507 (2013).
34. Loudet, C., Hanusse, P. & Poulin, P. Stokes drag on a sphere in a nematic liquid crystal. *Science* **306**, 1525 (2004).
35. Conkey, D. B., Trivedi, R. P., Pavani, S. R. P., Smalyukh, I. I. & Piestun, R. Three-dimensional parallel particle manipulation and tracking by integrating holographic optical tweezers and engineered point spread functions. *Opt. Express* **19**, 3835–3842 (2011).
36. Liu, Q., Yuan, Y. & Smalyukh, I. I. Electrically and optically tunable plasmonic guest-host liquid crystals with long-range ordered nanoparticles. *Nano Lett.* **14**, 4071–4077 (2014).
37. Mundoor, H. & Smalyukh, I. I. Mesostuctured composite materials with electrically tunable upconverting properties. *Small* **11**, 5572–5580 (2015).
38. Evans, J. S., Beier, C. & Smalyukh, I. I. Alignment of high-aspect ratio colloidal gold nanoplatelets in nematic liquid crystals. *J. Appl. Phys.* **110**, 033535 (2011).
39. Shah, R. R. & Abbott, N. L. Coupling of the orientations of liquid crystals to electrical double layers formed by the dissociation of surface-immobilized salts. *J. Phys. Chem. B* **105**, 4936–4950 (2001).
40. Smalyukh, I. I., Kaputa, D. S., Kachynski, A. V., Kuzmin, A. N. & Prasad, P. N. Optical trapping of director structures and defects in liquid crystals using laser tweezers. *Opt. Express* **15**, 4359 (2007).
41. Zhou, J. et al. Ultrasensitive polarized up-conversion of Tm³⁺–Yb³⁺ doped β-NaYF₄ single nanorod. *Nano Lett.* **13**, 2241–2246 (2013).
42. Yeh, P. & Gu, C. *Optics of Liquid Crystal Displays* (Wiley, 1999).
43. Weeks, E. R., Crocker, J. C., Levitt, A. C., Schofield, A. & Weitz, D. A. Three-dimensional direct imaging of structural relaxation near the colloidal glass transition. *Science* **287**, 627–631 (2000).
44. Anderson, V. J. & Lekkerkerker, H. N. W. Insights into phase transition kinetics from colloid science. *Nature* **416**, 811–815 (2002).
45. Gasser, U., Weeks, E. R., Schofield, A., Pusey, P. N. & Weitz, D. A. Real-space imaging of nucleation and growth in colloidal crystallization. *Science* **292**, 258–262 (2001).
46. Besseling, T. H. et al. Determination of the positions and orientations of concentrated rodlike colloids from 3D microscopy data. *J. Phys. Condens. Matter* **27**, 194109 (2015).
47. Hsiao, L. C. et al. Metastable orientational order of colloidal discoids. *Nat. Commun.* **6**, 8507 (2015).
48. Zheng, Z., Wang, F. & Han, Y. Glass transitions in quasi-two-dimensional suspensions of colloidal ellipsoids. *Phys. Rev. Lett.* **107**, 065702 (2011).
49. Mundoor, H., Senyuk, B. & Smalyukh, I. I. Triclinic nematic colloidal crystals from competing elastic and electrostatic interactions. *Science* **352**, 69–73 (2016).
50. Lee, T., Trivedi, R. P. & Smalyukh, I. I. Multimodal nonlinear optical polarizing microscopy of long-range molecular order in liquid crystals. *Opt. Lett.* **35**, 3447–3449 (2010).

Acknowledgements We thank M. Almansouri, B. Fleury, J. van de Lagemaat, Q. Liu, L. Longa, S. Park, B. Senyuk and J.-S. Tai for discussions and technical assistance. This research was supported by the US Department of Energy, Office of Basic Energy Sciences, Division of Materials Sciences and Engineering, under contract DE-SCO019293 with the University of Colorado at Boulder.

Author contributions H.M. synthesized disks and performed experiments and J.-S.W. performed Landau–de Gennes modelling of disk-induced distortions of the molecular order, under the supervision of I.I.S. H.H.W. designed the theoretical model and performed the numerical calculations of colloidal ordering of disks, with input from I.I.S. H.M. and I.I.S. analysed data. I.I.S. conceived, designed and directed the research, provided funding and wrote the manuscript, with input from all authors.

Competing interests The authors declare no competing interests.

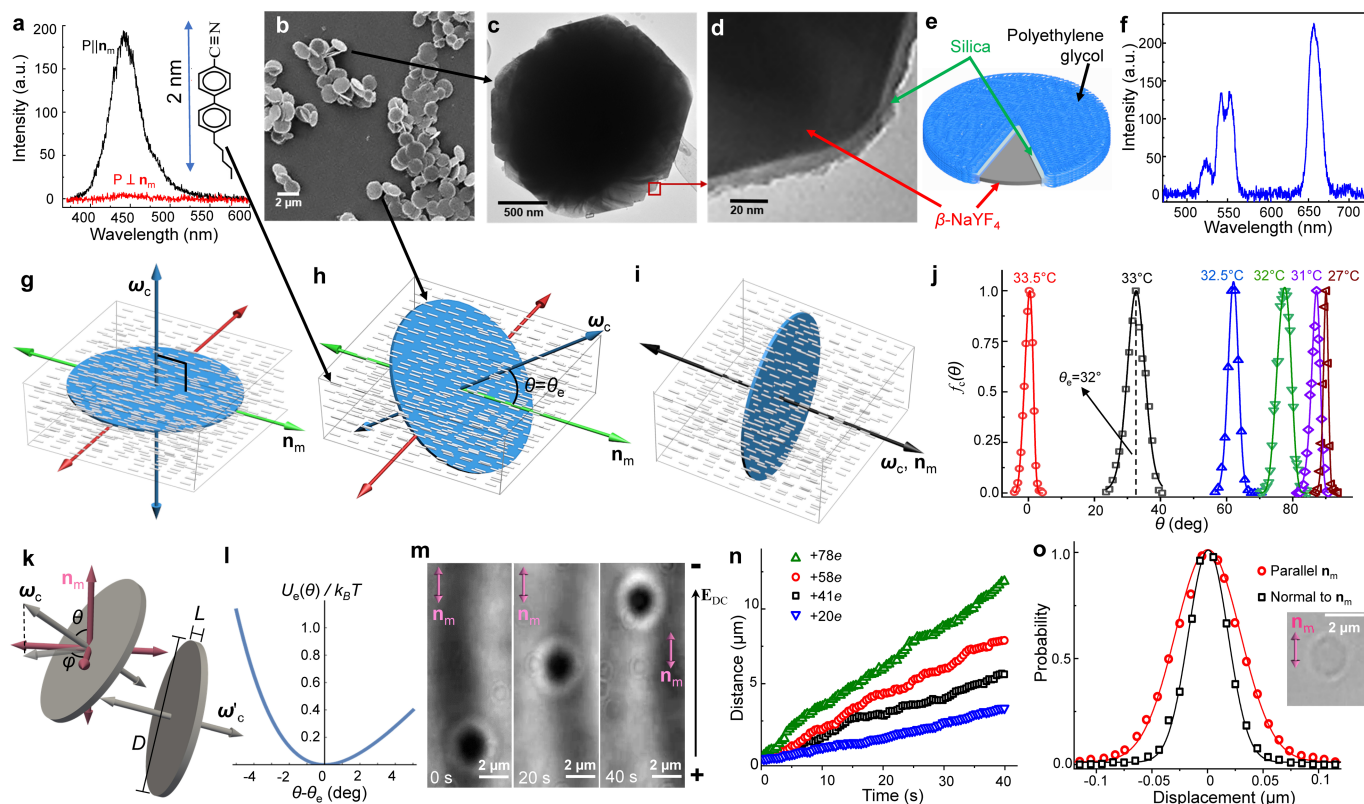
Additional information

Supplementary information The online version contains supplementary material available at <https://doi.org/10.1038/s41586-021-03249-0>.

Correspondence and requests for materials should be addressed to I.I.S.

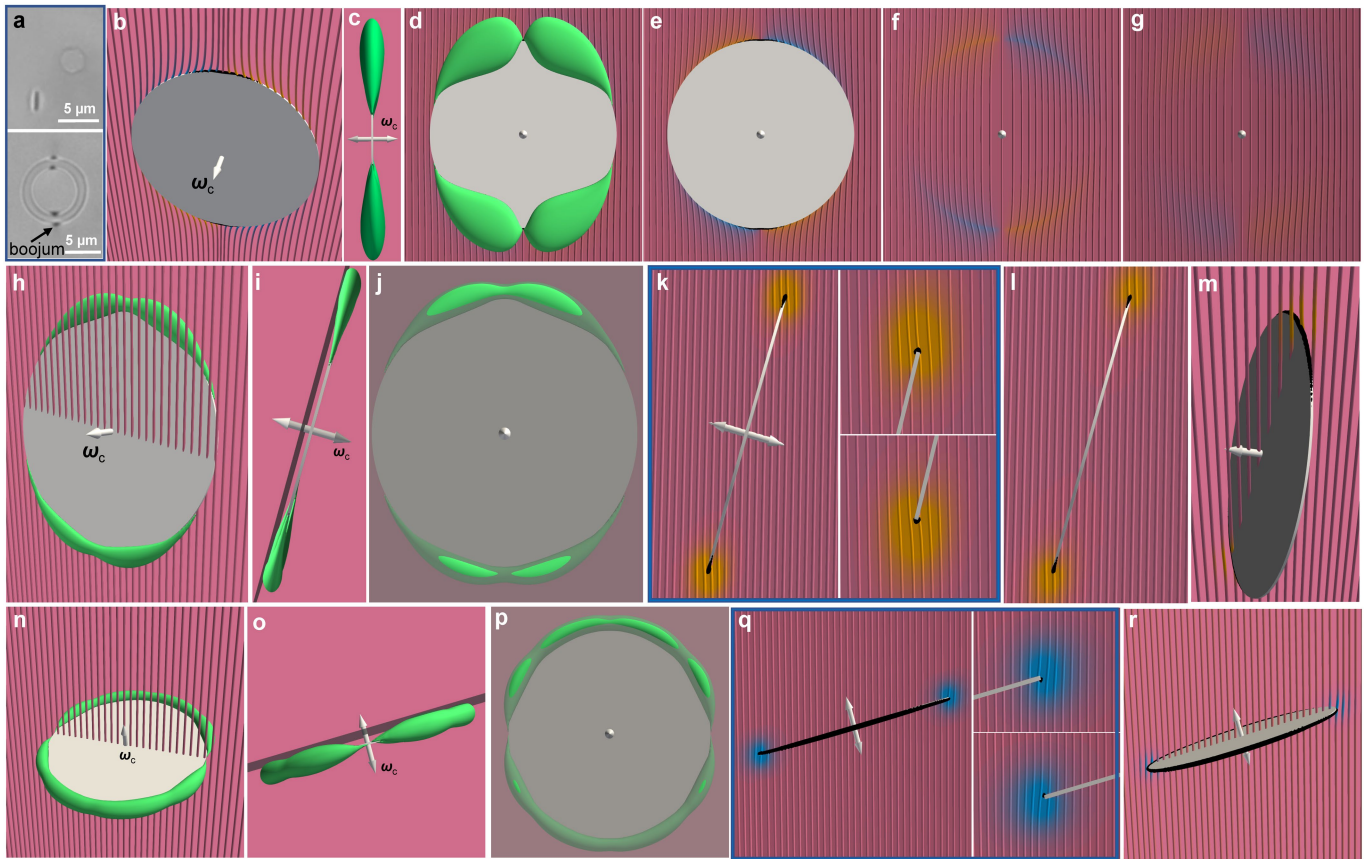
Peer review information Nature thanks Fulvio Bisi and the other, anonymous, reviewer(s) for their contribution to the peer review of this work.

Reprints and permissions information is available at <http://www.nature.com/reprints>.



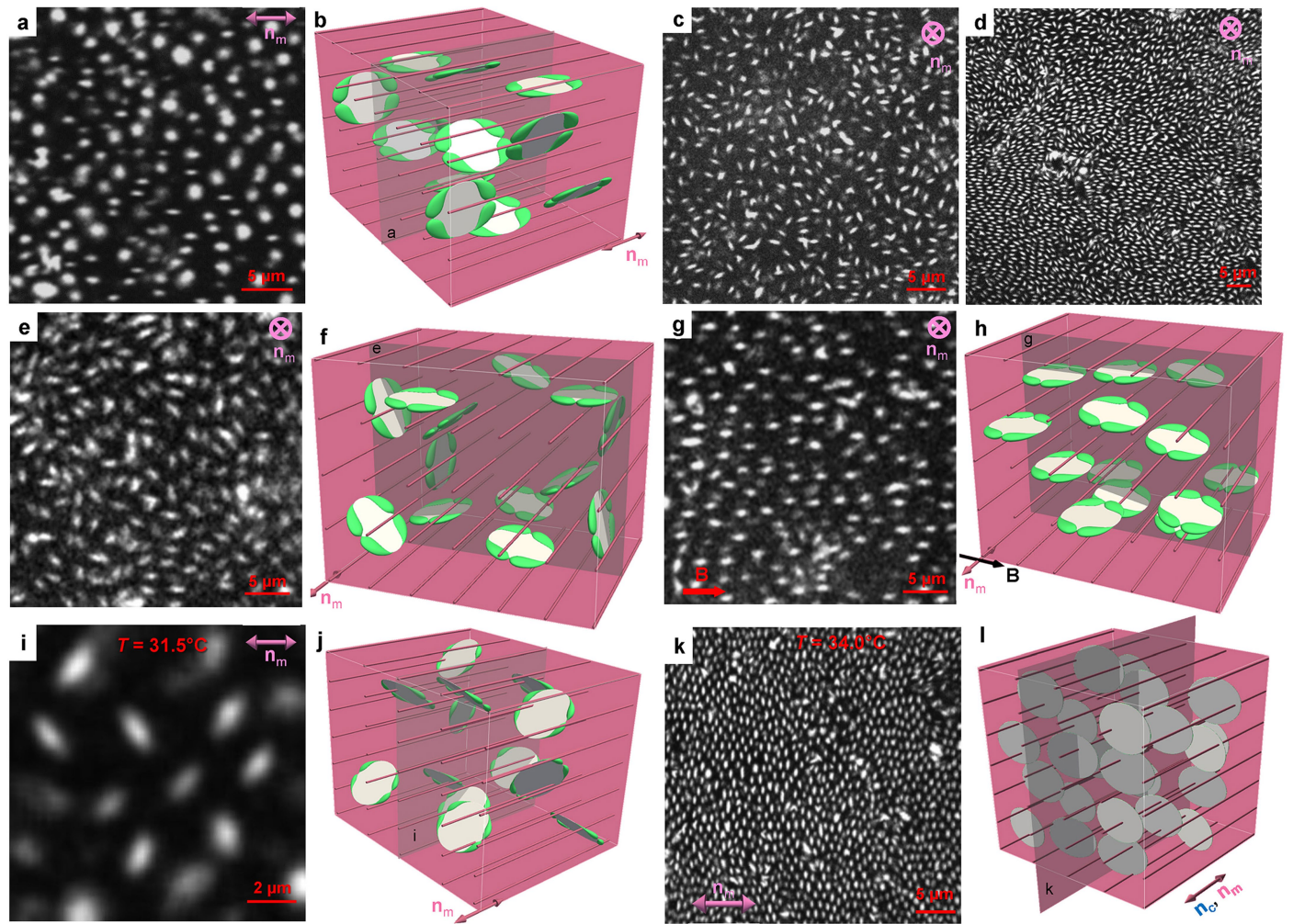
Extended Data Fig. 1 | Characterization of the building blocks of nematic colloids. **a**, Three-photon excitation fluorescence spectra of 5CB obtained for polarizations (**P**) of excitation light parallel and perpendicular to \mathbf{n}_m . The inset shows the chemical structure and length of a 5CB molecule. **b**, Scanning electron micrographs of silica-coated disks. **c**, Transmission electron micrograph image of a single disk on a copper grid. **d**, A zoomed-in view of the region in the red square in **c**, showing the silica layer. **e**, Schematic of a disk with the NaYF_4 core, silica layer and polyethylene glycol functionalization. **f**, Photon-upconverting luminescence spectrum of disks used in confocal imaging. **g–i**, Simplified schematics of an effective building block of a molecular–colloidal LC formed by a disk (blue) in a fluid host of molecular rods (grey), illustrating its orthorhombic (**g**), monoclinic (**h**) and uniaxial (**i**) symmetries at different orientations. **j**, Orientational probability versus θ at different T values marked next to the distributions. The peaks of the curves correspond to θ_e , as depicted with a black

dashed line at $\theta_e = 32^\circ \pm 1^\circ$ for $T = 33.0 \pm 0.1^\circ \text{C}$. The error in measuring θ is $\pm 1^\circ$. **k**, Schematics of the main notations. **l**, Asymmetry of the colloidal surface anchoring potential $U_e(\theta) \approx \varepsilon_2(\theta - \theta_e)^2 + \varepsilon_3(\theta - \theta_e)^3 + \varepsilon_4(\theta - \theta_e)^4$, plotted for $\varepsilon_2 = 88$, $\varepsilon_3 = -550$ and $\varepsilon_4 = 1,608$. **m**, Time-lapse bright-field micrographs of a disk in 5CB, showing its field-induced motion when subjected to an electric field \mathbf{E}_{DC} (black arrow) generated by a d.c. voltage of 5V applied to in-plane electrodes 1 mm apart. The elapsed time and \mathbf{n}_m orientations are marked on the micrographs. **n**, Displacement versus time for disks with different charges in 5CB when subjected to 5V between electrodes 1 mm apart. **o**, Histograms of the disk Brownian displacement probed along and perpendicular to \mathbf{n}_m using video microscopy, with the inset showing a bright-field micrograph of a disk in 5CB. Solid curves are Gaussian fits to experimental data. Errors in measuring the displacements in **n**, **o** are $\pm 10 \text{ nm}$. a.u., arbitrary units.



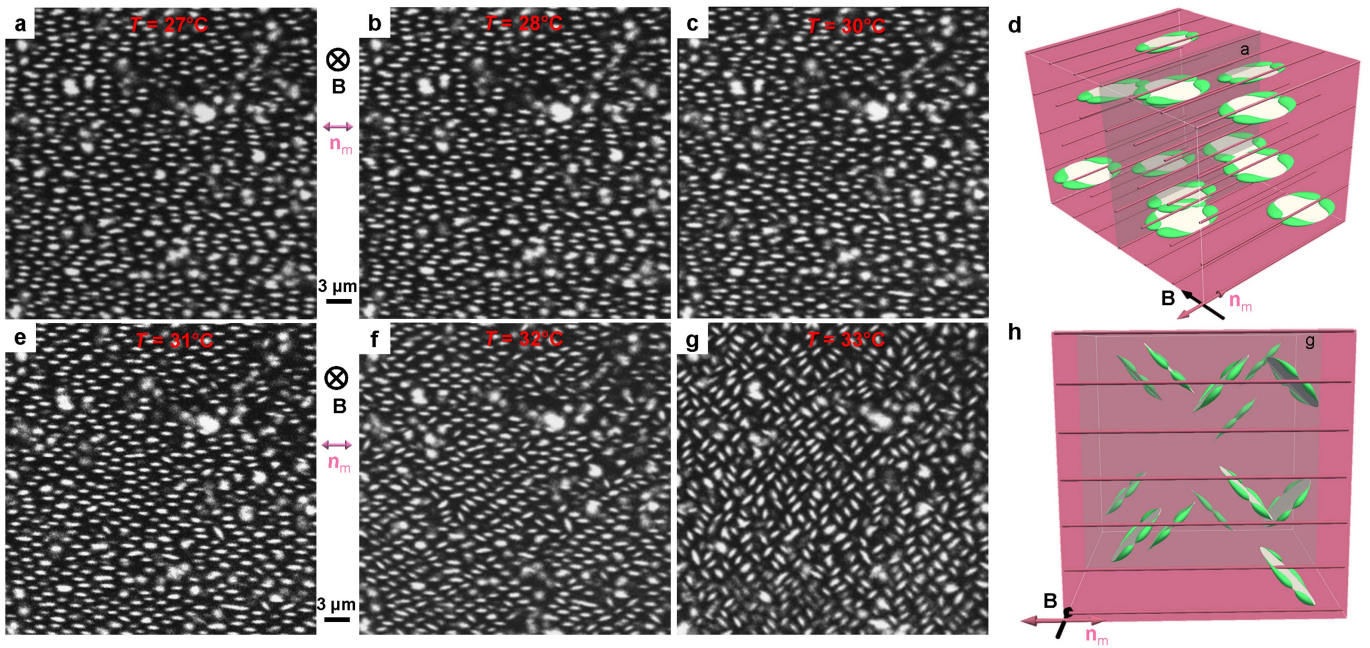
Extended Data Fig. 2 | Comparison and visualization of perturbed nematic order at different disk orientations. **a**, Comparison of colloidal particles with tangential surface boundary conditions shaped as thin disks with different orientations (top) and a microring (bottom) in SCB imaged by bright-field microscopy under similar conditions, with the latter inducing four boojum surface point defects visible as dark, light-scattering spots. No light-scattering singular defects are detected around the disks. **b–g**, Numerical modelling of \mathbf{n}_m distortions around a disk at $\theta_e = 90^\circ$. **b–d**, Visualization of energy-minimizing \mathbf{n}_m distortions around the disk, where the green isosurface-enclosed region indicates deviation of \mathbf{n}_m by $>2^\circ$ from its uniform far field and the black isosurface-enclosed region shows where S_m is reduced by $>5\%$ below its bulk equilibrium value. Colours of streamlines depict the opposite directions of local \mathbf{n}_m tilting relative to the midplane of the disk. **e–g**, \mathbf{n}_m distortions near the

same disk at 0 nm (**e**), 10 nm (**f**) and 50 nm (**g**) away from its midplane. **h–m**, Numerical modelling of a disk-induced \mathbf{n}_m corona at $\theta_e = 75^\circ$. **h–j**, Visualization of energy-minimizing \mathbf{n}_m distortions around the disk, where the green isosurface-enclosed region indicates deviation of \mathbf{n}_m by $>2^\circ$ from its uniform far-field background. The grey pane in **i, j** that intersects the green isosurfaces helps to show the monoclinic symmetry of \mathbf{n}_m distortions relative to the midplane of the disk. **k–m**, Isosurfaces enclosing small regions with S_m reduced by $>5\%$ below its bulk value (black surfaces) and colour-coded local \mathbf{n}_m distortions around the disk. Right-side insets in **k** depict details of nematic order perturbations at the disk edges. Field lines in **l** are shown 250 nm away from the disk centre and the single mirror-symmetry plane. **n–r**, Visualizations similar to **h–m**, but for $\theta_e = 30^\circ$. Note the opposite \mathbf{n}_m tilt at disk edges compared to that in **h–m**, as highlighted by orange/blue colouring.



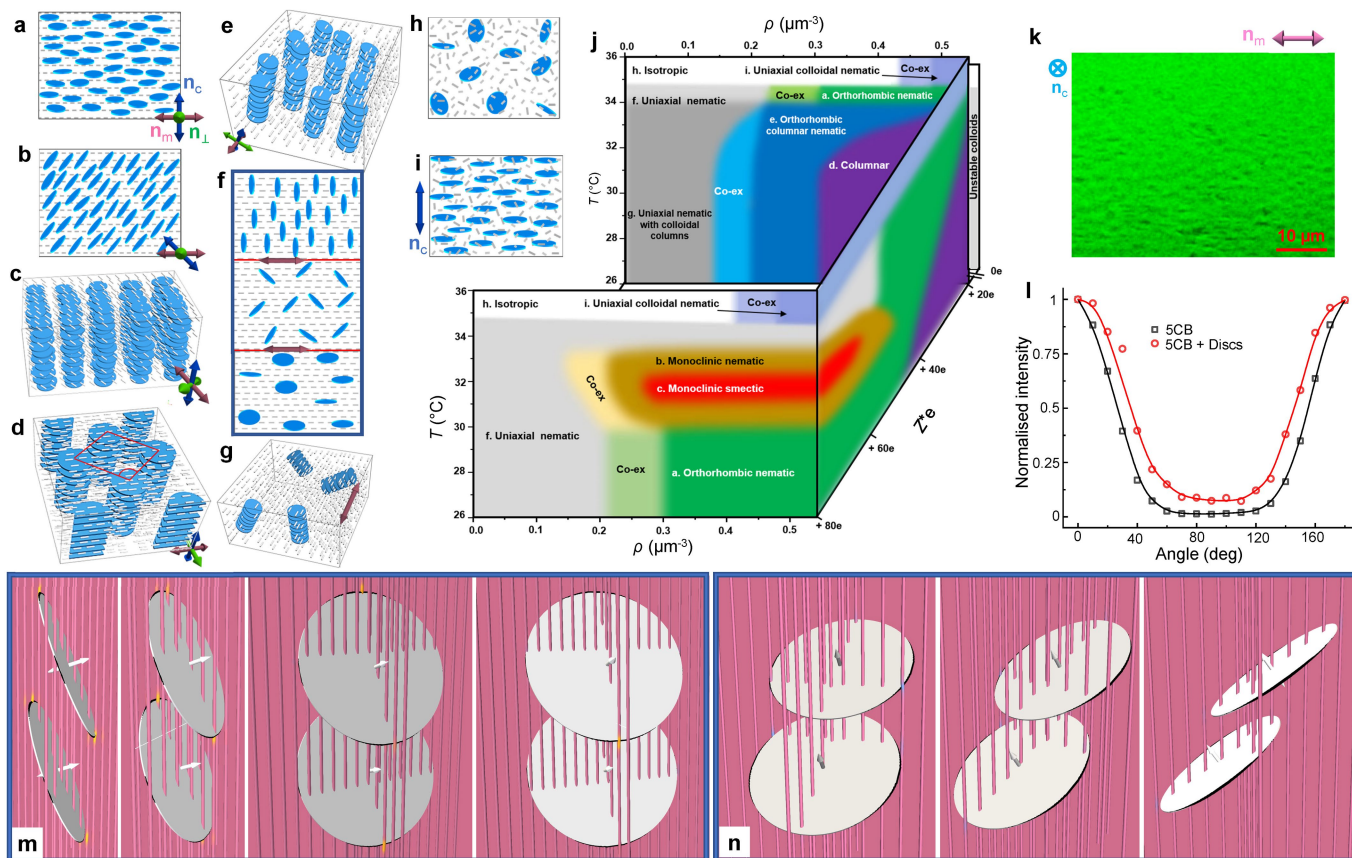
Extended Data Fig. 3 | Uniaxial nematic dispersions and magnetic field alignment of disks. **a–c**, Uniaxial nematic phase characterized by upconverting luminescence confocal images (**a**, **c**) and numerical visualization (**b**) for in-plane (**a**) and out-of-plane (**c**) \mathbf{n}_m , showing the random orientations of the disk normals ω_c in the plane perpendicular to \mathbf{n}_m . The orientation of the cross-sectional confocal image shown in **a** is depicted in **b** with a grey plane. **d**, Confocal image of a sample within a uniaxial–orthorhombic co-existence region with local correlations of ω_c orientations. The disk number density is

$\rho = 0.16 \mu\text{m}^{-3}$ (**a**), $\rho = 0.11 \mu\text{m}^{-3}$ (**c**) and $\rho = 0.21 \mu\text{m}^{-3}$ (**d**). **e–h**, Magnetic alignment of initially randomly oriented disk normals ω_c (**e**, **f**) to point perpendicular to both \mathbf{n}_m and \mathbf{B} at magnetic field amplitude $B = 100$ mT (**g**, **h**). Visualizations in **f**, **h** correspond to the images in **e**, **g**, respectively; $\rho = 0.09 \mu\text{m}^{-3}$ and $Z^*e \approx +80e$ in **e**, **g**. **i**, **j**, Confocal image (**i**) and numerical visualization (**j**) for a uniaxial nematic with disks oriented obliquely to \mathbf{n}_m at $T = 31.5 \pm 0.1$ °C and $\rho = 0.08 \mu\text{m}^{-3}$. **k**, **l**, Confocal image (**k**) and numerical visualization (**l**) of a uniaxial nematic at $\rho = 0.19 \mu\text{m}^{-3}$ and $T = 34.0 \pm 0.1$ °C.



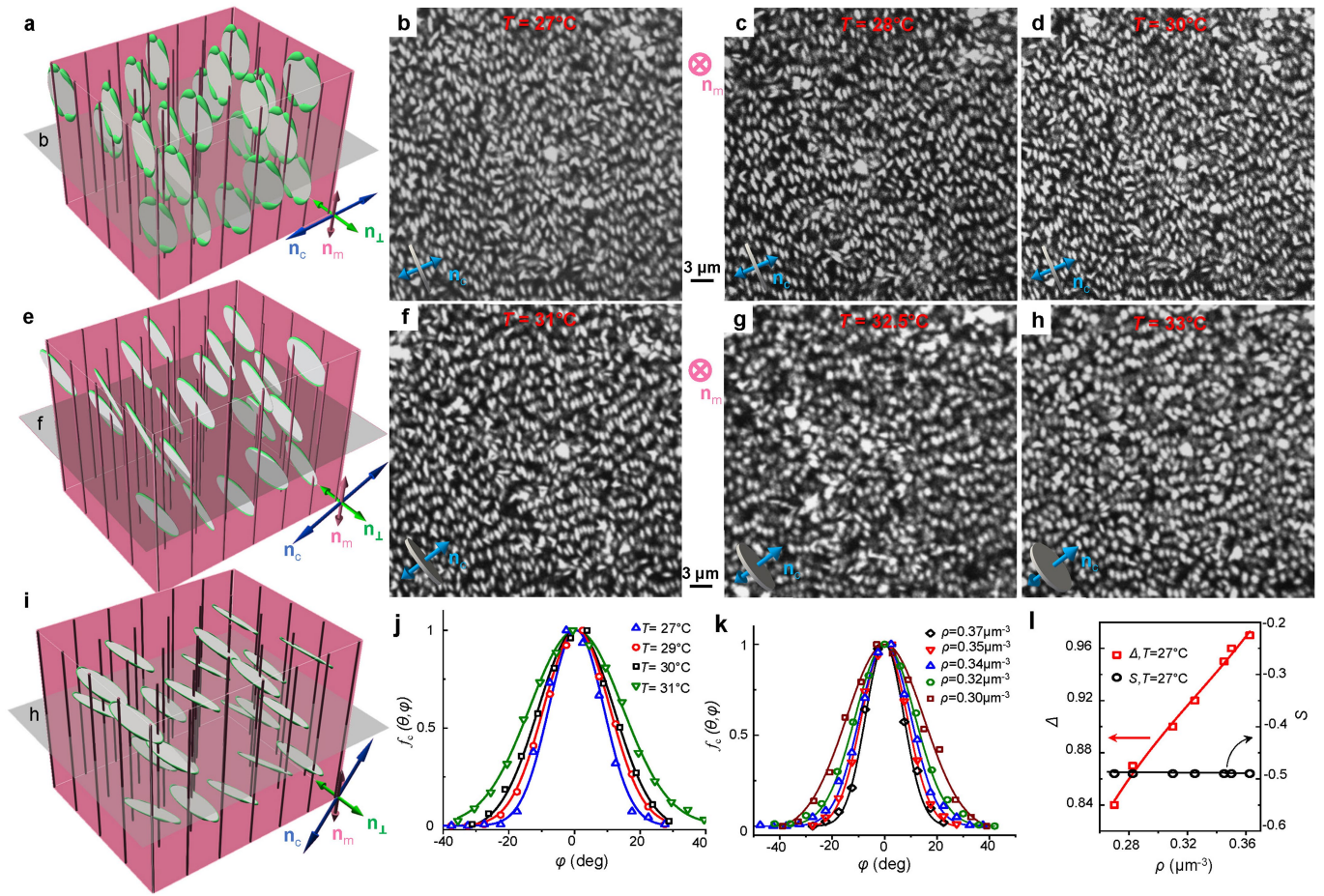
Extended Data Fig. 4 | Temperature-dependent orientations and magnetic control of disks. **a-h**, Upconversion-based luminescence confocal images (**a-c**, **e-g**) and corresponding numerical visualizations (**d**, **h**) of disk dispersions at $\rho = 0.19 \mu\text{m}^{-3}$ with in-plane \mathbf{n}_m and ω_c at $T = 27.0 \pm 0.1^\circ\text{C}$ (**a**), $T = 28.0 \pm 0.1^\circ\text{C}$ (**b**), $T = 30.0 \pm 0.1^\circ\text{C}$ (**c**), $T = 31.0 \pm 0.1^\circ\text{C}$ (**e**), $T = 32.0 \pm 0.1^\circ\text{C}$ (**f**) and $T = 33.0 \pm 0.1^\circ\text{C}$ (**g**), showing the temperature-dependent disk orientations in the presence of a magnetic field. With increasing T at a field of $B = 100 \text{ mT}$

applied along a normal to the sample, a domain with a magnetically induced unidirectional alignment of ω_c (**a-d**) transforms into a polydomain state at higher temperatures owing to the random $\pm\theta_c$ tilting directionality of ω_c relative to \mathbf{n}_m . Image planes are depicted in grey in **f-h**. The orientations of \mathbf{n}_m , magnetic field and scale bars shown between **a**, **b** and **e**, **f** are the same for all confocal images presented. The disk surface charge is $Z^*e \approx +80e$.



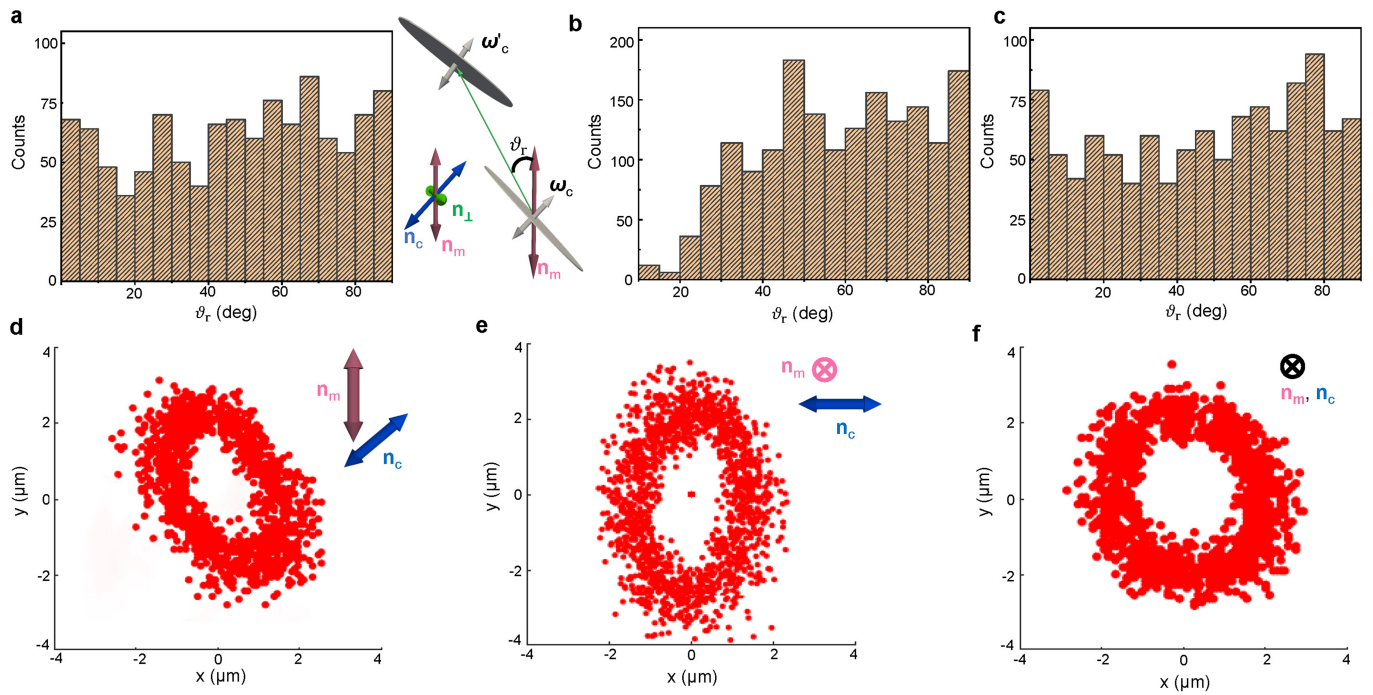
Extended Data Fig. 5 | Coarse-grained visualization of LC phases and background alignment. **a–i**, Simplified schematics of different hybrid phases of SCB molecular rods (grey) and colloidal disks (blue) for the orthorhombic nematic (**a**), monoclinic nematic (**b**), monoclinic smectic (**c**), columnar (**d**), orthorhombic columnar nematic (**e**), uniaxial nematic (**f**), uniaxial nematic with colloidal columns (**g**), isotropic (**h**) and colloidal nematic (**i**) states. An elementary columnar cell in **d** is depicted in red, with details shown in Fig. 5h. **j**, Phase diagram upon variation of ρ , T and Z^*e , with ‘Co-ex’ referring to co-existence regions. Disks aggregate at $Z^*e < +10e$ and form Wigner-type crystals at $Z^*e > +100e$ (ref. ¹⁰). T is measured with an error of $\pm 0.1^\circ$; relative

errors for ρ and Z^*e are $\pm 5\%$ and $\pm 1\%$, respectively. **k**, 3PEFPM image of a SCB dispersion of disks at $\rho = 0.32 \mu\text{m}^{-3}$ and $T = 27.0 \pm 0.1^\circ\text{C}$ for linear polarization of the excitation light parallel to \mathbf{n}_m . **l**, 3PEFPM intensity, averaged over the field of view, versus the angle between the linear polarization of the excitation light and \mathbf{n}_m (measured with an error of less than $\pm 1^\circ$) for SCB with colloidal disks and pure SCB under the same conditions. **m, n**, Visualization of \mathbf{n}_m between two disks at $\theta_e = 75^\circ$ (**m**) and $\theta_e = 30^\circ$ (**n**), with black isosurfaces enclosing spatial regions in which S_m is reduced by $>5\%$ relative to its equilibrium bulk value. Regions of distorted \mathbf{n}_m are highlighted by coloured streamlines, with blue and yellow depicting opposite tilt directions.



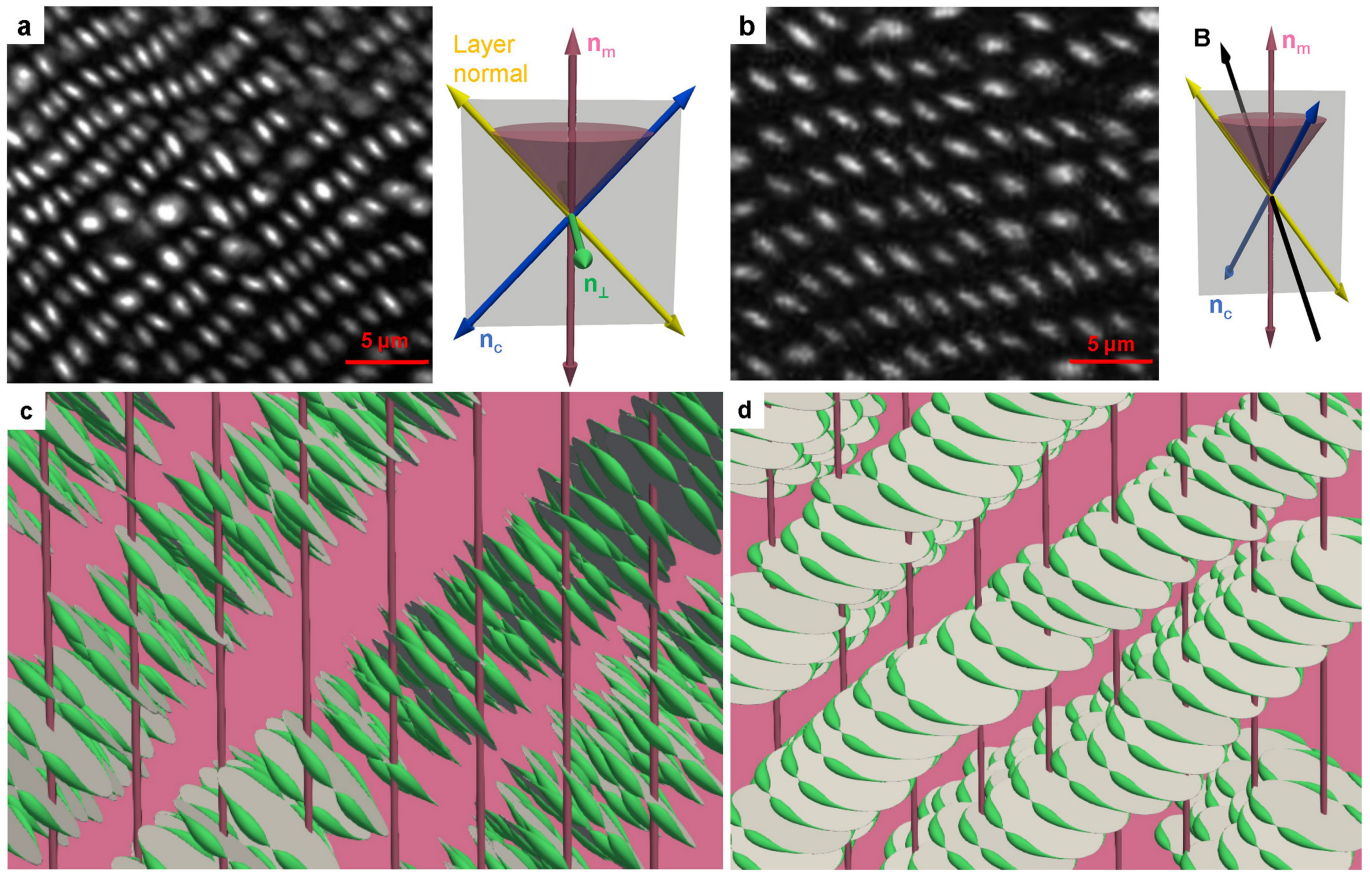
Extended Data Fig. 6 | Colloidal director rotation and nematic ordering versus temperature. **a–i**, Numerical visualizations (**a, e, i**) and upconversion-based luminescence confocal images (**b–d, f–h**) of disks in the monoclinic and orthorhombic nematic phases with out-of-plane \mathbf{n}_m at disk number density $\rho = 0.31 \mu\text{m}^{-3}$ and at $T = 27.0 \pm 0.1^\circ\text{C}$ (**b**), $T = 28.0 \pm 0.1^\circ\text{C}$ (**c**), $T = 30.0 \pm 0.1^\circ\text{C}$ (**d**), $T = 31.0 \pm 0.1^\circ\text{C}$ (**f**), $T = 32.5 \pm 0.1^\circ\text{C}$ (**g**) and $T = 33.0 \pm 0.1^\circ\text{C}$ (**h**). Note the pretransitional smectic correlations in the vicinity of the smectic phase temperature range in **f, g**. \mathbf{n}_c tilts out of the sample plane owing to the temperature-dependent variation of θ_{ne} , consistent with the elliptical

cross-section of disks, revealing oblique orientations of ω_c and \mathbf{n}_c relative to \mathbf{n}_m at $T = 32.5 \pm 0.1^\circ\text{C}$ (**g**) and $T = 33.0 \pm 0.1^\circ\text{C}$ (**h**). Grey planes in **a, e, i** depict the orientation of confocal images relative to the directors. Scale bars and \mathbf{n}_m orientation shown between panels **b, c** and **f, g** are the same for all images. **j**, $f_c(\theta, \varphi)$ versus azimuthal angle φ of ω_c at $\rho = 0.34 \mu\text{m}^{-3}$ and different T values. **k**, $f_c(\theta, \varphi)$ versus φ at $T = 27.0 \pm 0.1^\circ\text{C}$ for different ρ values. **l**, Δ (red squares) and S (black circles) versus ρ at $T = 27.0 \pm 0.1^\circ\text{C}$. The disk surface charge is $Z^*e \approx +80e$.



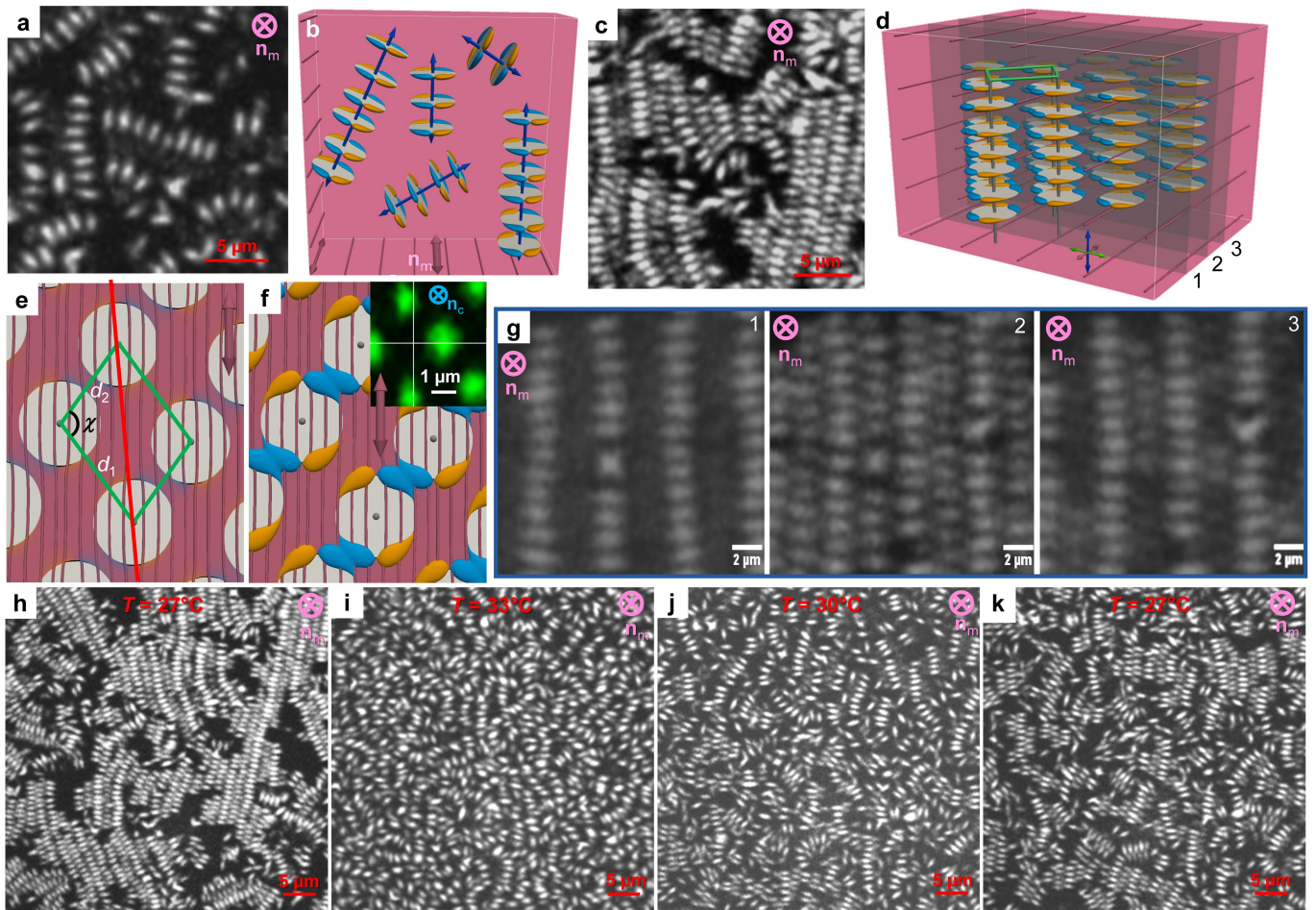
Extended Data Fig. 7 | Characterization of colloidal interactions within different phases. a–c, Distribution of the angle θ_r between \mathbf{n}_m and the centre-to-centre pair separation vector, defined in the right-side inset of **a**, in the monoclinic nematic at $\rho = 0.31 \mu\text{m}^{-3}$ and $T = 30.7 \pm 0.1^\circ\text{C}$ (**a**), orthorhombic nematic at $\rho = 0.34 \mu\text{m}^{-3}$ and $T = 27.0 \pm 0.1^\circ\text{C}$ (**b**) and uniaxial nematic at

$\rho = 0.1 \mu\text{m}^{-3}$ and $T = 27 \pm 0.1^\circ\text{C}$ (**c**). The error in measuring θ_r is $\pm 2^\circ$. **d–f,** Scatter plots of the nearest-neighbour disk positions in the monoclinic (**d**), orthorhombic (**e**) and uniaxial (**f**) nematic phases at ρ and T values corresponding to **a–c**. Anisotropic distributions in **d** and **e** correlate with the ordering of disks. The disk surface charge is $Z^*e \approx +80e$.



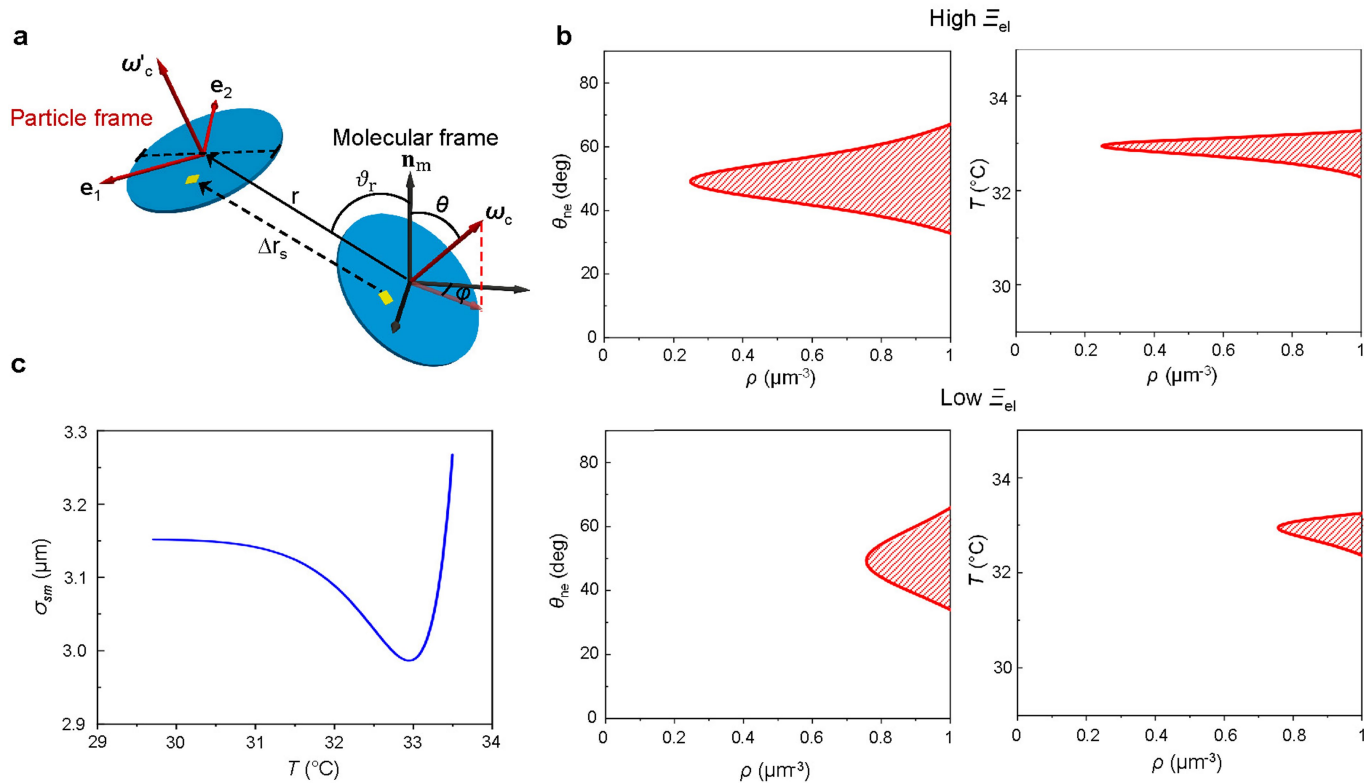
Extended Data Fig. 8 | Monoclinic and magnetic-field-induced triclinic smectic order. **a–d**, Upconversion-based luminescence confocal microscopy images (**a, b**) and numerical visualizations (**c, d**) of disks in the monoclinic smectic phase at $\rho \approx 0.3 \mu\text{m}^{-3}$, $T = 32.3 \pm 0.1 \text{ }^\circ\text{C}$ and $\theta_{\text{nc}} \approx 45^\circ$ (**a, c**) and for the magnetically induced triclinic smectic state under otherwise similar conditions (**b, d**). The smectic layer normal (yellow double arrow), \mathbf{n}_c and \mathbf{n}_m are initially within the image plane (**a, c**), but then \mathbf{n}_c is rotated out of the image plane by a magnetic field of $B = 100 \text{ mT}$ (**b**), thus switching the smectic order

from monoclinic (**a, c**) to triclinic (**b, d**). This switching is driven by the tendency of ω_c and \mathbf{n}_c to align perpendicular to \mathbf{B} , where the disk normals also tend to reside on a cone of anchoring-defined easy-angle ω_c orientations. Right-side insets of **a, b** show the layer normal, \mathbf{n}_m , \mathbf{n}_c and \mathbf{n}_\perp and the applied magnetic field \mathbf{B} for the monoclinic and the triclinic smectic states, respectively. The layer normal, \mathbf{n}_c and \mathbf{n}_\perp are all mutually orthogonal and the layer normal, \mathbf{n}_c and \mathbf{n}_m are all co-planar in **a** but not in **b**, which lacks nontrivial symmetry operations and represents triclinic symmetry.



Extended Data Fig. 9 | Nematic and columnar phases and their thermal melting. **a–c**, Upconversion-based luminescence confocal micrographs (**a**, **c**) and numerical visualization (**b**) showing a uniaxial nematic with differently oriented columns at $\rho = 0.08 \mu\text{m}^{-3}$ and $T = 27.0 \pm 0.1 \text{ }^\circ\text{C}$ (**a**, **b**) and the colloidal structure of the biphasic nematic–columnar co-existence region at $\rho = 0.17 \mu\text{m}^{-3}$ and $T = 27.0 \pm 0.1 \text{ }^\circ\text{C}$ (**c**). **d–g**, Monoclinic columnar phase with a two-dimensional oblique lattice characterized experimentally (**f**, **g**) and numerically (**d–f**). The inset in **f** shows the ordering of columns in a sample with out-of-plane \mathbf{n}_c and in-plane \mathbf{n}_m , revealing the oblique lattice of colloidal columns. Probing the distribution of the oblique lattice parameters defined in **e** across multiple sample regions yields angles of $\chi = 110^\circ \pm 5^\circ$; $d_1 = 1.67 \pm 0.15 \mu\text{m}$, $d_2 = 1.75 \pm 0.15 \mu\text{m}$. The angle between the diagonal of the oblique primitive cell

and \mathbf{n}_m varies within 5° – 7° . The measuring error is $\pm 1^\circ$ for angles and $\pm 50 \text{ nm}$ for d_1 and d_2 . Coloured \mathbf{n}_m director streamlines in **e** depict \mathbf{n}_m distortions right above the disks. Orange/blue isosurfaces in **f** enclose regions in which local \mathbf{n}_m orientation departs from its uniform far-field background by $>2^\circ$, with colours corresponding to the tilt directionality of the streamlines in **e**. **g**, Confocal cross-sections of the columnar phase showing disks at sample depths shifted by $2 \mu\text{m}$ sequentially, corresponding to the grey planes labelled in **d**; $\rho = 0.32 \mu\text{m}^{-3}$ and $T = 27.0 \pm 0.1 \text{ }^\circ\text{C}$. **h**, **i**, Confocal photon-upconverting images of disks at $\rho = 0.19 \mu\text{m}^{-3}$ that show melting of the colloidal columns upon increasing the temperature from $T = 27.0 \pm 0.1 \text{ }^\circ\text{C}$ (**h**) to $T = 33.0 \pm 0.1 \text{ }^\circ\text{C}$ (**i**). **j**, **k**, Columns re-emerge upon decreasing T , as revealed by confocal images at $T = 30.0 \pm 0.1 \text{ }^\circ\text{C}$ (**j**) and $T = 27.0 \pm 0.1 \text{ }^\circ\text{C}$ (**k**). The disk charge is $+20e$.



Extended Data Fig. 10 | Stability analysis of phases with partial positional order. **a**, Schematic showing the principal reference frames, vectors and angles. **b**, Phase diagrams with coordinate axes θ_{ne} versus ρ (left column) and T versus ρ (right column) of the molecular-colloidal LC for higher (0.002; top row) and lower (0.001; bottom row) values of the elastic energy Ξ_{el} (renormalized in units of thermal energy) that quantifies the relative strength of elastic attractions with respect to steric repulsion (Supplementary

Information). Red-shaded regions represent the monoclinic smectic phase, consistent with the experimental diagram (Fig. 2a). For lower Ξ_{el} (weak elastic interactions), the phases with partial positional order appear at higher disk concentrations owing to stronger electrostatic repulsions between the disks. **c**, Theoretical estimation of the smectic layer spacing σ_{sm} versus T in the monoclinic smectic phase.